MIT 3.3 GHz RELATIVISTIC KLYSTRON AMPLIFIER: EXPERIMENTAL STUDY OF INPUT CAVITY AND BEAM CHARACTERISTICS

by

Palmyra E. Catravas

B.S. in Electrical Engineering, University of Maryland, 1991
B.M. in Music, University of Maryland, 1991

Submitted to the
Department of Electrical Engineering and Computer Science
in Partial Fulfillment of the Requirements for the
Degree of

MASTER OF SCIENCE

at the

MASSACHUSETTS INSTITUTE OF TECHNOLOGY

May, 1994

Signature of Author_____
Department of Electrical Engineering and Computer Science
May 13, 1994

Certified by_____
George Bekefi, Professor of Physics
Thesis Supervisor

Accepted by_____
Frederic R. Morgenthaler, Chairman
Committee on Graduate Students

MIT 3.3 GHz RELATIVISTIC KLYSTRON AMPLIFIER: EXPERIMENTAL STUDY OF INPUT CAVITY AND BEAM CHARACTERISTICS

PALMYRA CATRAVAS

Submitted to the Department of Electrical Engineering and Computer Science
on May 13, 1994, in Partial Fulfillment of the
Requirements for the
Degree of
Master of Science in Electrical Engineering

Abstract

Recent research has shown that the high current relativistic klystron with an annular electron beam is an excellent high power microwave source. Advances in RKA design at higher frequencies are of practical interest. Experimental work on the input stage of a 3.3 GHz relativistic klyston amplifier will be reported. We designed and tested a compact, tunable reentrant input cavity and studied the current modulation it produces. In the experimental set-up, the Nereus Marx Accelerator provides a 5 kA, 350 kV, 150 ns annular electron beam, which is confined with a 1-2 T guide field from a superconducting magnet. Up to 1 MW is available at 3.1-3.5 GHz from a tunable magnetron. The power is injected radially to the cavity through a single C-band coupling aperture. Studies of the current modulation as a function of input power, axial position, beam current and guide field strength will be described. We observed about 5% current modulation downstream from the cavity gap, in good agreement with theory and MAGIC simulations.

Thesis Supervisor: George Bekefi, Professor of Physics

Acknowledgments

I would like to express my respect and admiration for Professor George Bekefi and thank him for the chance to work in his laboratory. His teaching and guidance are invaluable to me.

This project relied heavily on the engineering expertise and insightful suggestions of Ivan Mastovsky. Students speak of Ivan not only for his technical help, but for the moral support and encouragement he gives each of us.

Sincere thanks to Chiping Chen for his many suggestions and generous hours of patient explanations and discussions of RKA theory.

I wish to express my thanks to Wen Hu, and acknowledge his penetrating insights, creative ideas and long hours of work on the RKA.

A special thanks to Felicia Brady, a member of the laboratory who is a person of extraordinary talent and inner qualities.

Many thanks and good wishes to Professor Jonathan Wurtele, Jim Blastos, Beth Chen, Manoel Conde, Todd Hay, Ken Ricci, David Sisson, Gennady Shvets, Rick Stoner and Paul Volfbeyn. I am indebted to Rick Stoner and Manoel Conde for sharing their knowledge and experience.

Most of all, I thank my family for their love and support.

This material is based upon work supported under a National Science Foundation Graduate Research Fellowship.

Outline

CHAPTER ONE

Introduction

Over the past five decades, electron beam devices have evolved from low power prototypes to intense radiation sources, opening doors in diverse areas of application. Current research seeks to drive frequency and power to higher limits in order to advance work in accelerator physics, radar and directed energy, and radio-biology. New vistas in applications to microelectronics, spectroscopy and magnetic fusion also open as high power sources develop.

Through the years, the klystron has been one of the most reliable and successful of the electron beam devices when intermediate and high power microwaves are required. For future applications, especially massive-scale undertakings in which a large number of microwave sources are expected to operate in tandem, the klystron's high efficiency, and good amplitude and phase stability are essential attributes, and it competes well with the numerous high power devices under development. Klystrons can also be designed for wide bandwidth, although this property has yet to be achieved at the highest power levels.

In one direction of current research, relativistic klystrons patterned after conventional klystrons are being scaled to high power by increasing beam energy. Like the conventional klystrons, they contain pencil beams at sufficiently low current that space charge forces are negligible. In 1985, 100 MW output levels were reached with a klystron of this genre at 2.856 GHz, 415 kV, 1 μsec, 48% efficiency at SLAC. A study of output

power scaling with beam voltage and frequency has been pursued at SLAC for frequencies up to 11.4 GHz [Benford, 1992].

Recently, however, a different movement in klystron research was initiated when pulsed power levels at the gigawatt level were achieved for the first time in a new regime of klystron operation. This class of klystron employs a high current, relativistic annular electron beam. New physics issues arise as characteristic currents approach the limiting current and space charge forces become considerable. The first klystron of this type was designed by Friedman and Serlin at NRL, who reported gigawatt pulse powers at 1.3 GHz in 1985. Comprehensive papers documenting experimental and theoretical work to date are available [Friedman, 1985; Lau, 1990; Colombant, 1991; Krall, 1991].

Many issues remain to be resolved in RKA research. Breakdown and pulse shortening problems afflict klystron designs and become increasingly pronounced at higher frequencies. Improvement in input and output power coupling is critical if wall-plug efficiencies are to be made practical for large-scale use. The interesting physics of the high current regime of klystron operation is not fully investigated. We are designing and building an RKA at 3.3 GHz to study these questions further. The experiment can also be used to explore the novel Two Stream RKA concept [Chen, 1993].

Work performed on the input section of the 3.3 GHz RKA will be described in this thesis. Chapter 2 contains a summary of basic RKA theory. Calculations of the relation between fields and current modulation necessary for studies of bunching are included. In particular, the range of validity of the analytical expressions is investigated with the aid of the PIC code MAGIC. Chapter 3 covers the experimental setup, and documents an upgrade

of the Nereus Marx Accelerator. Chapter 4 describes cavity cold tests and studies of beam bunching by the input section. Results are compared with simulations and theory.

CHAPTER 2

Theory

2.1 The Basic Klystron Amplification Mechanism

In a klystron amplifier, a configuration of independent, resonant cavities excites longitudinal space charge waves on an electron beam and extracts power from the bunched beam (Figure 2.1). Input power is fed to the leading cavity, which applies a longitudinal RF electric field across the beam. The alternating field modulates the beam

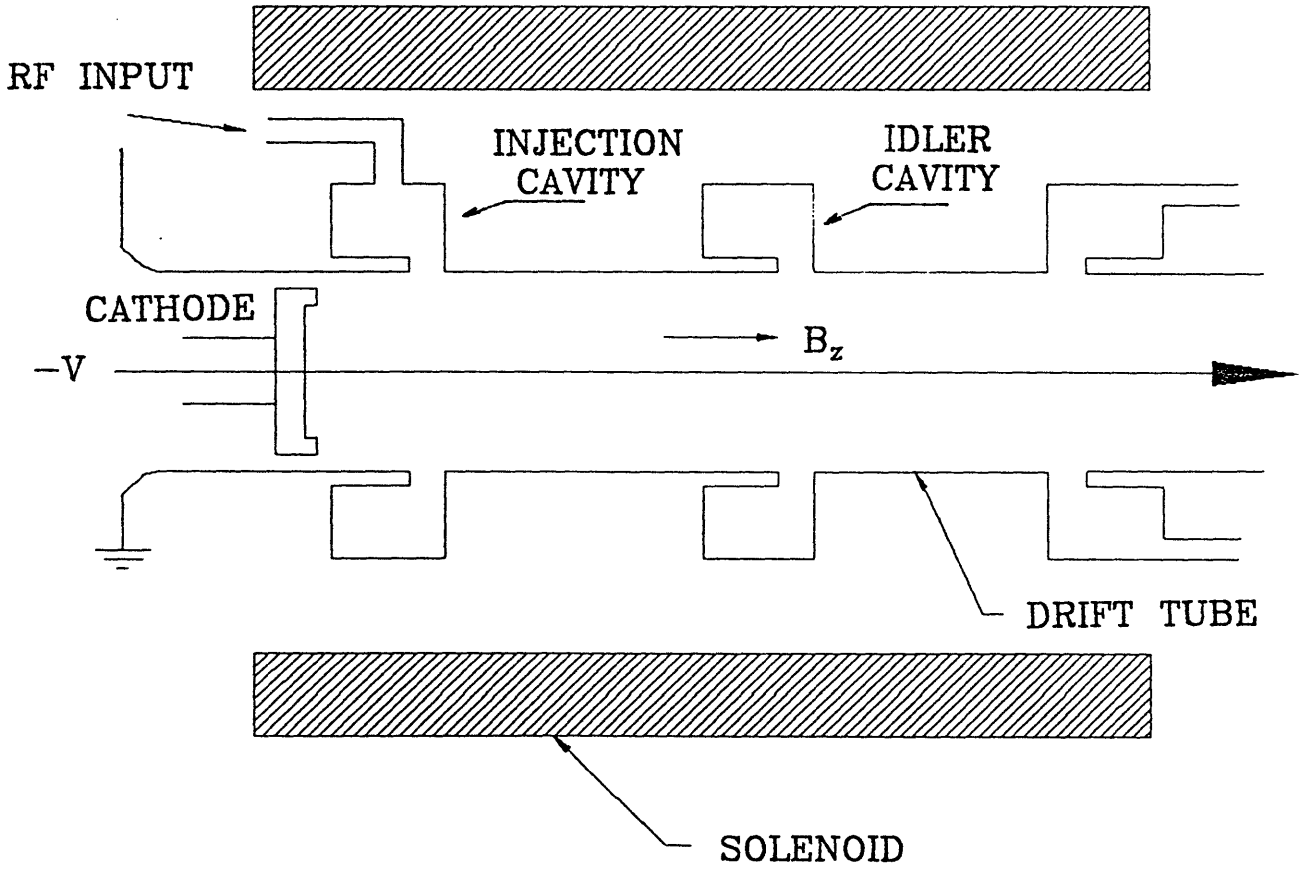

Figure 2. 1 *Schematic of RKA.*

velocity at the cavity gap, leading to current modulation downstream. In order to enhance the modulation, one or more passive cavities may follow the input cavity. The bunched beam passing through these intermediate cavities excites the resonant mode at the operating frequency and the fields act back on the beam to intensify the bunching. In order that the cavities be independent, the cylindrical drift tube radius in which the beam propagates is such as to prohibit electromagnetic wave propagation at the klystron frequency. Energy is extracted from the beam at the output cavity, where the fields excited by the highly bunched beam are out of phase with the current modulation. The RF power coupled out of the cavity taps the reservoir of DC beam power. Therefore, if a small amount of input RF can produce strong modulations on a beam that has a large average kinetic energy, there is potential for high power gain from the device.

2.2 RKA Theory and Design Issues

The following section surveys basic RKA theory, emphasizing design issues. Since the RKA operates with high currents and a mildly relativistic electron beam, space charge forces govern the beam dynamics. The role of space charge forces in defining the output power level and the spatial characteristics of current modulation will be discussed.

The model. An infinitely thin annular beam with radius a confined by an infinite guide magnetic field propagates with velocity v in a smooth, cylindrical drift tube of radius b. Thus, longitudinal modes are treated, while velocity shear effects and azimuthal modes

are not. In the strong magnetic field imposed, transverse electron motion can be neglected.

2.2.1 Conservation of Energy and Limiting Current.

Conservation of energy arguments show that the beam current is bounded by the limiting current, I_L [Briggs, 1976]:

$$I_L = I_o(\gamma_{inj}^{2/3} - 1)^{3/2}$$

where $I_0 = \dfrac{2\pi\varepsilon_0 m_0 c^3}{e\ln(\frac{b}{a})} = \dfrac{8.5kA}{\ln(\frac{b}{a})}$

m_0 = electron rest mass

and γ_{inj} refers to normalized relativistic injection energy, $m_o c^2(\gamma_{inj} - 1)$.

At the current I_L both the group and phase velocities of the slow space charge wave on the beam go to zero for small wavenumbers, and the beam cannot propagate in the drift tube. Thus, the product $V_b I_b$ cannot be indefinitely augmented by simply forcing an arbitrarily high current into the drift tube. Space charge effects place a ceiling on DC beam power. Operation near the limiting current, however, is believed to enhance the klystron bunching mechanism [Lau, 1990]. partition

Conservation of energy states that the total energy given to the beam at injection is partitioned between kinetic and potential energy:

$$\gamma_{inj} = \gamma + \frac{I_b}{\beta I_0}$$

At sufficiently high beam currents, the portion of the total beam energy stored as potential energy no longer remains negligible compared to kinetic energy. The work done by the beam at the output cavity gap, $\bar{E} \cdot \bar{J}$, springs from the kinetic energy of the beam. Thus, as the current is raised higher and higher, the proportion of the injection energy that supplies useful work decreases. For our nominal RKA operating parameters, potential energy makes up 25% of the total energy, while for a classical klystron the figure is negligibly small. In sum, space charge effects limit the contribution that the DC beam power can make to the amplification process.

2.2.2 Spatial characteristics of beam bunching.

Long wavelength approximation. The RF excitation at the cavity gap induces plasma oscillations on the moving beam at a reduced plasma frequency determined by the geometry and boundary conditions. For long waves much longer than the drift tube radius b, the longitudinal space charge waves excited on the beam obey the following dispersion relation in the long wavelength limit [Briggs, 1976]

$$D(\omega, k_z) = 1 - \frac{\varepsilon(c^2 k_z^2 - \omega^2)}{(\omega - k_z v)^2} = 0$$

where D is the dielectric coefficient, and ε is proportional to the square of the plasma frequency ω_p. The quantity ε can be expressed in terms of geometry, beam current I_b, and beam β and γ. It is defined as:

$$\varepsilon = \frac{I_b}{\beta\gamma^3 I_0}$$

In general, ε is very much less than unity, and typically between 0.1 and 0.01. Solving for the wavenumbers of the fast and slow wave on the beam for a given RF excitation at ω gives:

$$\frac{k_z}{\omega} = \frac{\beta \pm \sqrt{(1+\varepsilon)\varepsilon - \beta^2 \varepsilon}}{c(\beta^2 - \varepsilon)}$$
$$\cong \frac{1}{v} \pm \frac{\sqrt{\varepsilon}}{\beta \gamma^3 c} \qquad \text{for } \varepsilon << 1.$$

Thus, the spatial characteristics of the current modulation are given by the beating of the two space charge waves as shown in Figure 2.2, with approximate characteristic mean and beat wavelengths ($\varepsilon << 1$):

$$\lambda_{mean} \cong \frac{v}{f}$$
$$\lambda_{rel} \cong \frac{1}{f} \frac{\gamma \beta^2 c}{\sqrt{\varepsilon}} = \lambda_{mean} \frac{\gamma \beta}{\sqrt{\varepsilon}},$$

where $\omega = 2\pi f$. The spatial period of the modulation envelope λ_{rel} is inversely related to the reduced plasma frequency.

Full dispersion relation. High beam currents shift the RKA operating point toward shorter space charge wavelengths. Outside the long wavelength regime, that is, when the wavelength becomes comparable or smaller than the drift tube radius, the space charge waves obey the dispersion relation [Lau, 1987] for the case of the TM_{01} mode of our cylindrical drift tube:

$$D(\omega, k_z) = 1 - \frac{\varepsilon R(c^2 k_z^2 - \omega^2)}{(\omega - k_z v)^2} = 0$$

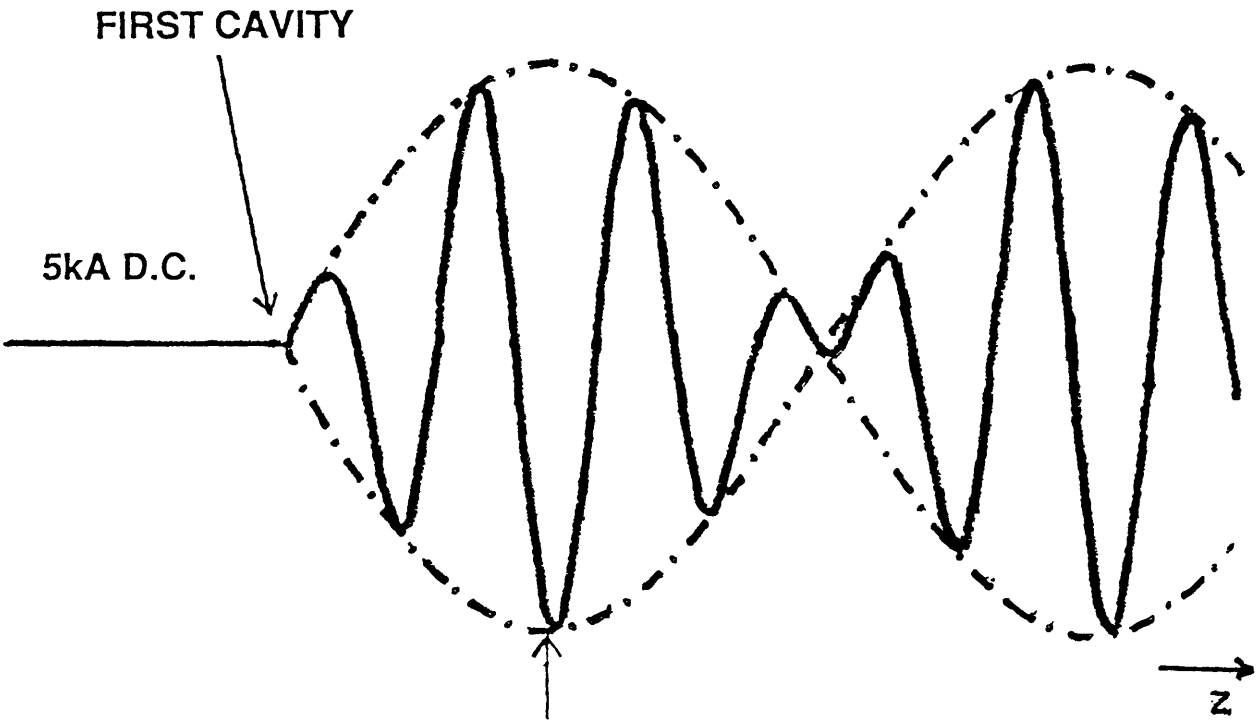

Figure 2. 2 *Expected current modulation after the first cavity.*

where the quantity ε has been reduced by the factor R, a function of ω, k_z and geometry.

$$R = \frac{1}{\ln(\frac{a}{b})} \frac{I_0(pa)}{I_0(pb)} \left[I_0(pa)K_0(pb) - I_0(pb)K_0(pa) \right]$$

with $p^2 = k_z^2 - (\omega/c)^2$. For $pa << 1$, R approaches 1 and the long wavelength dispersion relation is recovered. A plot of the dispersion relations both with and without the long wavelength restriction is shown in Figure 2.3, where the nominal operating point for our experiments is labeled. For our experimental parameters (eV_{inj}=350kV, a=1.9cm, b=2.37cm, f=3.383GHz, I_b=5kA), R~0.8 and the predicted distance to the beat maximum falls from a value of 9 cm to a value of 7.5 cm (that is, the error due to the long wavelength approximation is about 16%.)

In summary, high klystron output power levels require high DC beam power, $V_b I_b$. The limiting current puts an absolute bound on I_b in the klystron, but can potentially exert a positive effect on the bunching mechanism. Choosing the annular beam configuration positioned close to the wall maximizes current and distributes the kinetic and potential energy of the beam most favorably for high power gain. Although both the geometric configuration and the high beam energy tend to increase the beat wavelength, the increase in allowed current counterbalances this effect.

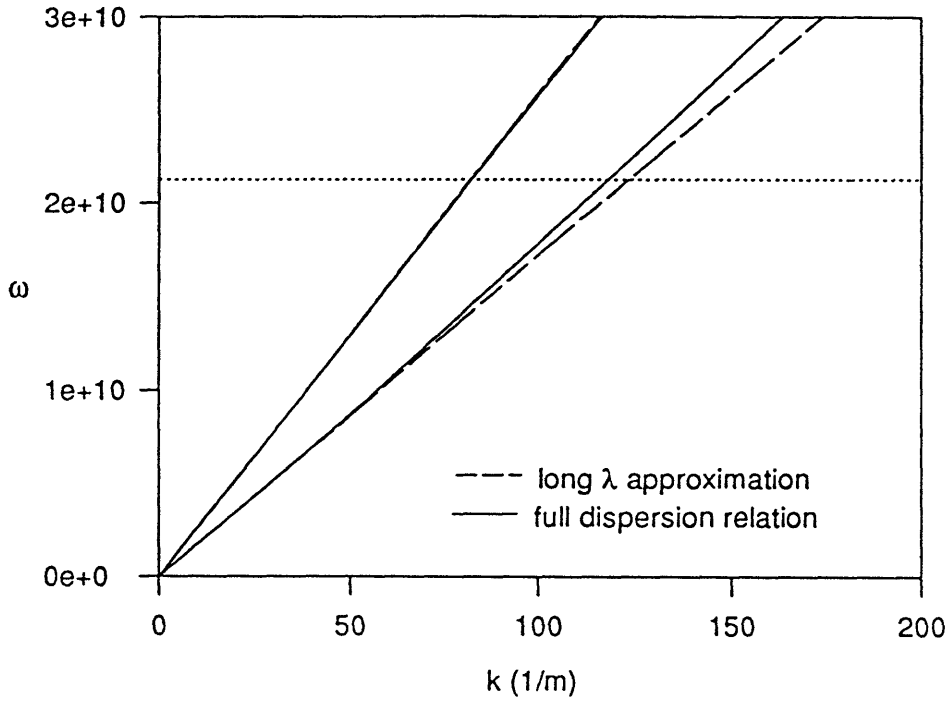

Figure 2. 3 *Dispersion relation for thin annular beam propagating in infinite drift tube. Parameters:* eV_{inj}*=350kV, a=1.9cm, b=2.37cm,* I_b*=5kA. The horizontal line represents our operating parameters.*

CHAPTER 3

Experimental Setup

The goal of experiments on the input stage of the RKA was to study the properties of the input cavity and of the beam bunching it creates. In the principal experimental set-up, the Nereus Accelerator produces an annular electron beam of 5 kA, 350 kV and 150 ns. Power from a 0.5-1 MW magnetron is injected into a reentrant cavity, coupling to a mode that produces a longitudinal RF field at the cavity gap. Guided by a 1-2 Tesla magnetic field from a superconducting magnet, the beam passes through the cavity gap and propagates down a drift region. Electric and magnetic dipole probes lining the drift tube monitor current modulation arising from the interaction of the beam and the fields at the gap. Incident and reflected power from the cavity are measured with directional couplers.

The sections below describe the components of this set-up in more detail.

3.1 The Nereus Accelerator.

The Nereus Marx Accelerator has been used by several generations of students in this laboratory for relativistic electron beam experiments [Hinshelwood, 1985]. However, in order to produce a beam with the appropriate parameters for RKA experiments, an upgrade was performed on Nereus. In particular, a new pulse-forming line, main switch, and diode insulating section were constructed.

3.1.1 Basic Principle.

Marx generators, a staple of high voltage pulse technology, are characterized by high energy storage, low output resistance, and low internal inductance. They typically fire high voltage, high current, fast risetime pulses into a low impedance load. Initially, a set of n capacitors in the Marx charge in parallel to a voltage V. On closure of interconnecting switches, the capacitors stack in series to discharge a voltage nV through the load. The charging resistors are orders of magnitude higher than the load resistance, so they are effectively open during discharge. Marx generators exploit the large increase in breakdown voltage under pulse conditions compared to DC. Thus, an n-stage Marx need only withstand breakdown at 1/n times the output voltage.

The Marx of the Nereus Accelerator [Clark, 1971] contains twelve 50 kV, 25 μF capacitors. The rated energy storage capacity is 3.75 kJ. The capacitors are arranged in a + - V configuration (Figure 3.1). The Marx then obtains the output of a 12-stage circuit with the advantages of a 6-stage Marx. The six switches consist of pairs of cylindrical electrodes separated by about one inch and pressurized with SF_6. The Marx is fired by sending 50 kV trigger pulses to needle electrodes in the switches of the first and second stages. The six individually housed switches replace the switch configuration of the original Nereus, which contained spherical electrodes in two common housings.

The Marx is connected to a pulse forming line, which shapes the Marx output into a 150-200 ns flat-topped, 20 ns risetime pulse. The pulse forming line is a simple, water-filled coaxial transmission line connected to the diode via a self-breaking switch. The PFL

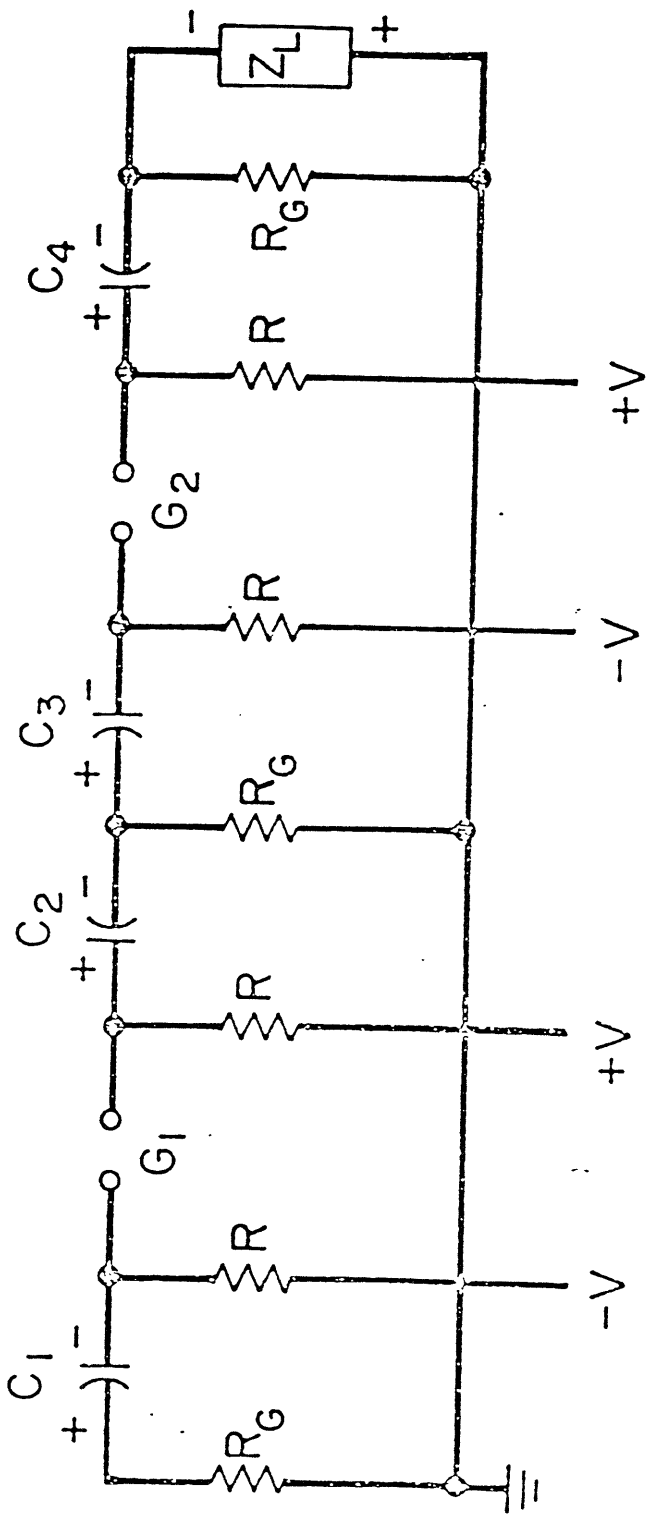

Figure 3. 1 *Simplified Marx circuit [Clark, 1971]*

charges like a lumped capacitor while the main switch remains open. After the switch breaks, the PFL behaves as a transmission line, producing a flat pulse of width equal to the round-trip time of the line. The use of distilled water in the line (ε_r=80) increases the pulse width and energy storage by a factor of nine over air for the same length PFL. The allusion to the Greek god Nereus is all the more appropriate for the upgraded accelerator, since over 300 gallons of water fill the new PFL.

The need for a new PFL arose because the interesting physics and useful output of the RKA cannot be reached with the original 30 ns beam pulse. This width is less than the cold fill time of the cavity. Table 3.1 compares the characteristics of the current PFL and the original line. The length of the inner conductor from Marx to main switch was increased from 2 to 10 feet, for a new pulse length of $\geq$150 ns. The characteristic impedance was changed from 2 to 8 ohms. A new main switch consists of a pair of self-breaking brass electrodes, pressurized with SF_6. Designed by I. Mastovsky, the optimized main switch produces the nearly ideal flat-topped pulse shown in Figure 3.3. In the original Nereus, the switch consisted of a 1/2 inch thick slab of Teflon, which needed to be replaced after every shot. The diode insulating section is also new, and was designed with the help of Los Alamos National Laboratory.

Water purity is critical to the operation of the PFL at such high voltages. A circulation system pumps the water through a pair of filters, where its resistivity is monitored. With the circulation system in operation about 75% of the time, Nereus was operated for about a year without changing the water. When the line was finally opened,

Table 3. 1 *Nereus Accelerator Upgrade*

MARX BANK
12 Capacitors - 0.25μF each
Maximum charging voltage V_M = 50 kV
Series Marx capacitance C_M = 20 nF
Maximum Stored Energy = 3750 kJ

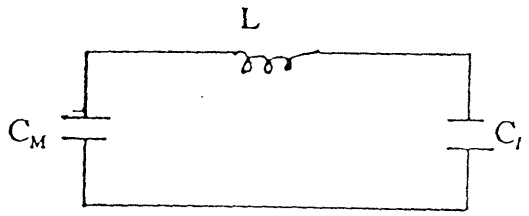

PULSE FORMING LINE (ε = 80)

PARAMETERS	PRESENT	UPGRADED
length $< l >$	24.0"	120"
2b	11.63"	28.0"
2a	8.63"	8.63"
C_l	9.02 nF	9.61 nF
$2C_M/(C_M+C_l)$	1.378	1.351
V_{Load}	413 kV	405 kV
Z	1.99Ω	7.89Ω
L	36.6 nH	599 nH
2τ	35.8 ns	152 ns
MAXIMUM PEAK POWER AVAILABLE	1.1×10^{11}W	2.5×10^{10}W

the interior surfaces needed no cleaning. This was a favorable improvement over the original pulse forming line, in which an additive was required to prevent growth of algae in the water and cleaning and water change were necessary every few weeks.

3.1.2 Diagnostics and Calibration of Marx Voltage.

Marx voltage was measured with two voltage diagnostics, as shown in Figure 3.2. A resistive divider across the final Marx stage monitors total Marx voltage after trigger and the charging up of the pulse forming line. A second diagnostic is located at the load end of the transmission line, after the main switch. Physically suspended across the diode insulating section, it measures voltage across the diode. Typical waveforms are shown in Figure 3.3.

In the process of debugging the upgraded Nereus, it was deemed necessary to perform an additional calibration of the Marx output voltage using a method independent of the diagnostics described above. This was done by terminating the pulse forming line with a matched load and measuring total current. Building and calibrating the load with sufficient precision was unexpectedly challenging. In the process, we improved the quality of our diagnostics and increased our understanding of their limitations.

The issues faced in building the matched load are not encountered in liquid resistive dividers. Traditionally, high power resistors are made from solutions of copper sulfate or sodium thiosulfate and resistance is calibrated with an AC bridge. Over time, highly resistive deposits precipitate on the brass or copper electrodes. The rate at which the deposits are formed depends on the concentration of ions in solution, and is

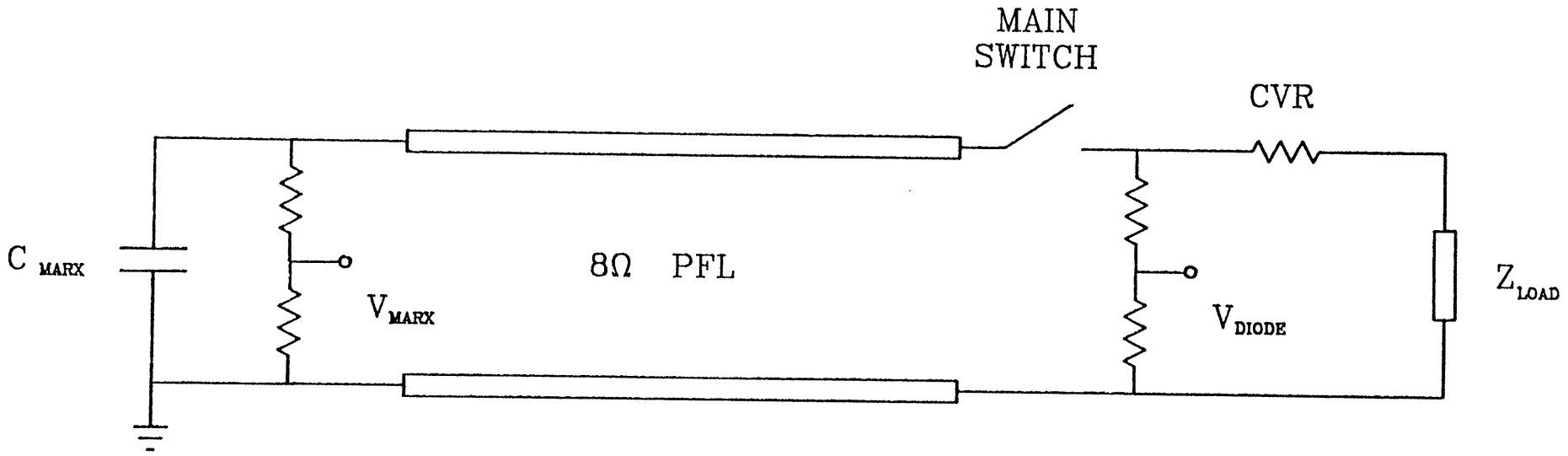

Figure 3. 2 *Nereus Accelerator voltage and current diagnostics.*

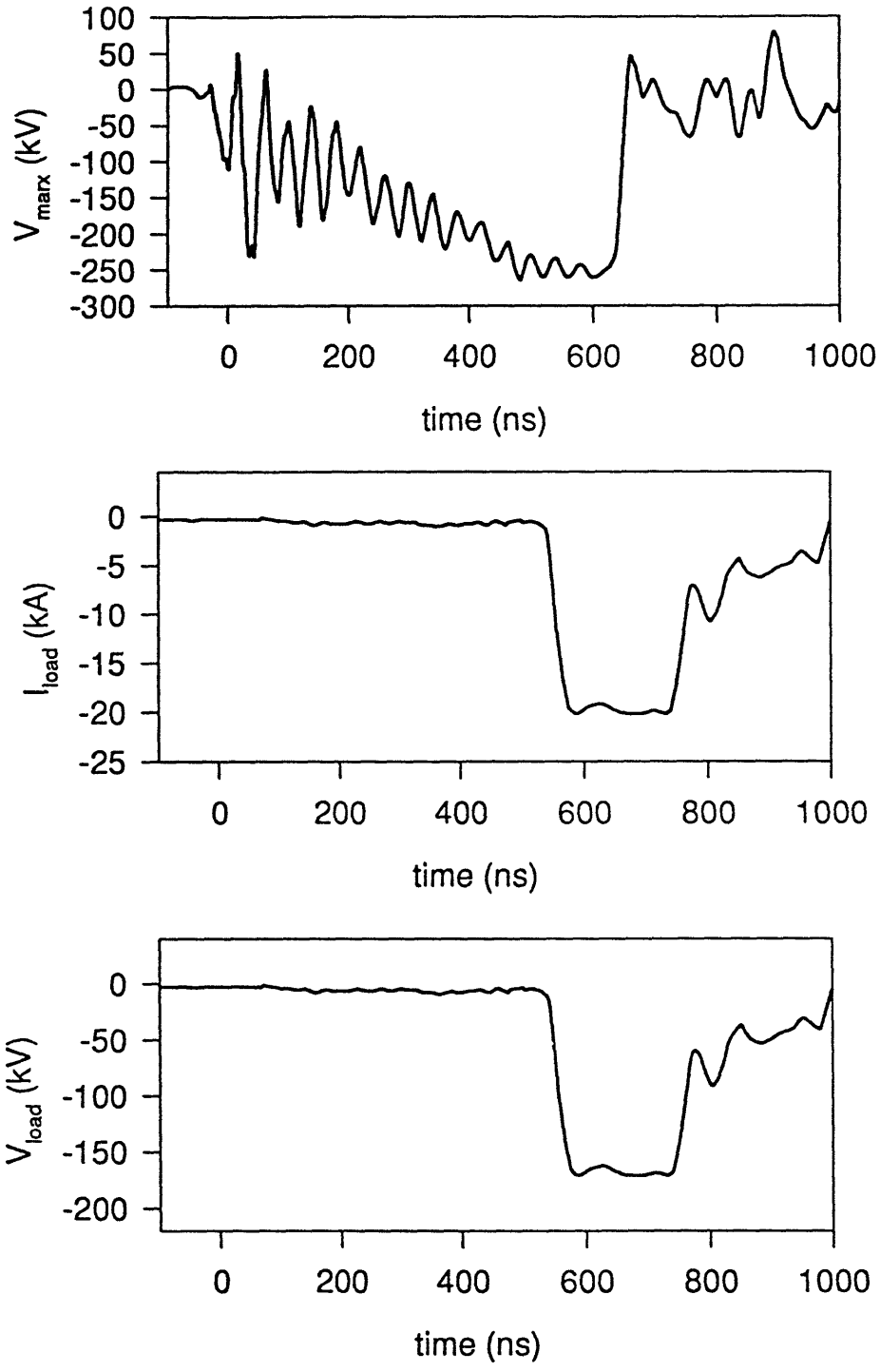

Figure 3. 3 *Upgraded Nereus output into a matched load: voltage across the final Marx capacitor (V_{marx}), load current and voltage.*

accelerated by the application of an applied voltage. We found that the 8 ohm resistance changed by 10% with each AC bridge measurement. Further investigation revealed that even the application of a single μsec pulse was sufficient to form some deposit. For voltages used during calibration (<100 V), the voltage drop across the deposit can be significant, while at Marx voltages (>100 kV) the deposits break down. Furthermore, it is possible that the entire stored energy of the Marx (up to 3.75 kJ) slams into matched load in 150 ns. Liquid resistors have even been known to boil and explode under these circumstances. In any case, the temperature and frequency dependence of the resistivity, combined with deposit resistance effects, can create such a large uncertainty in the load resistance value that it makes a poor calibration reference. It should be noted that these problems are circumvented by the geometry of liquid dividers as long as the solution can flow between the two sections of the divider. Changes in resistance due to temperature or frequency effects cancel in the ratio of resistances. At the kV level, the ratio should not include deposit effects and is determined by the electrode geometry alone. No measurements are really required. The calibration of the 8 Ω load presents some irregular difficulties.

Following a suggestion from D. Hinshelwood, whose thesis work in this laboratory in 1985 involved Nereus, a change of the solute to dry laundry detergent solved the problem. (Detergent in liquid suspension reacted with the electrode material and was more sensitive to temperature.) Deposits did not hamper the calibrations. Even high conductivity solutions could be calibrated with an AC bridge. Marx calibration results from the matched load agreed with diode divider measurements to within 15%.

Afterwards, the solution in the diode voltage divider was replaced with the same detergent. The resistances remained stable to within 10% after a year of shots at full voltage. The rise-time, however, is slightly less sharp than with the $CuSO_4$.

3.1.3 Current measurements

Diode design. A cold emission knife edge cathode and annular anode were used in main experiments (see Figure 3.4). Both were machined from Poco graphite. Beam radius is about 1.9 cm in the uniform field. The anode has an inner radius equal to the drift tube radius (2.37 cm) and an outer radius of 2". The diode presents a mismatched load to the transmission line.

Total current flowing through the load was calibrated separately with two current viewing resistors (CVR's) of different design. The positions of the CVR's are shown in Figure 3.5. The output of each CVR is the voltage drop across a known, small resistance inserted in the return path of the current. The CVR must be designed to have good high frequency response at kA currents. The first CVR, a commercial model, is made of a cylindrical block of high conductivity material having a total resistance of 0.0009734 Ω. A witness plate (for example, a graphite disk) intercepts the electron beam, and the collected current passes to ground via the CVR and drift tube. The second CVR is made of 104 1/4 W carbon resistors in parallel, soldered in cylindrical symmetry between two brass flanges. CVR2 is of annular shape and is mounted in to the system like an extra flange in between the cavity and the transmission line. Its total resistance of 0.001 ohms

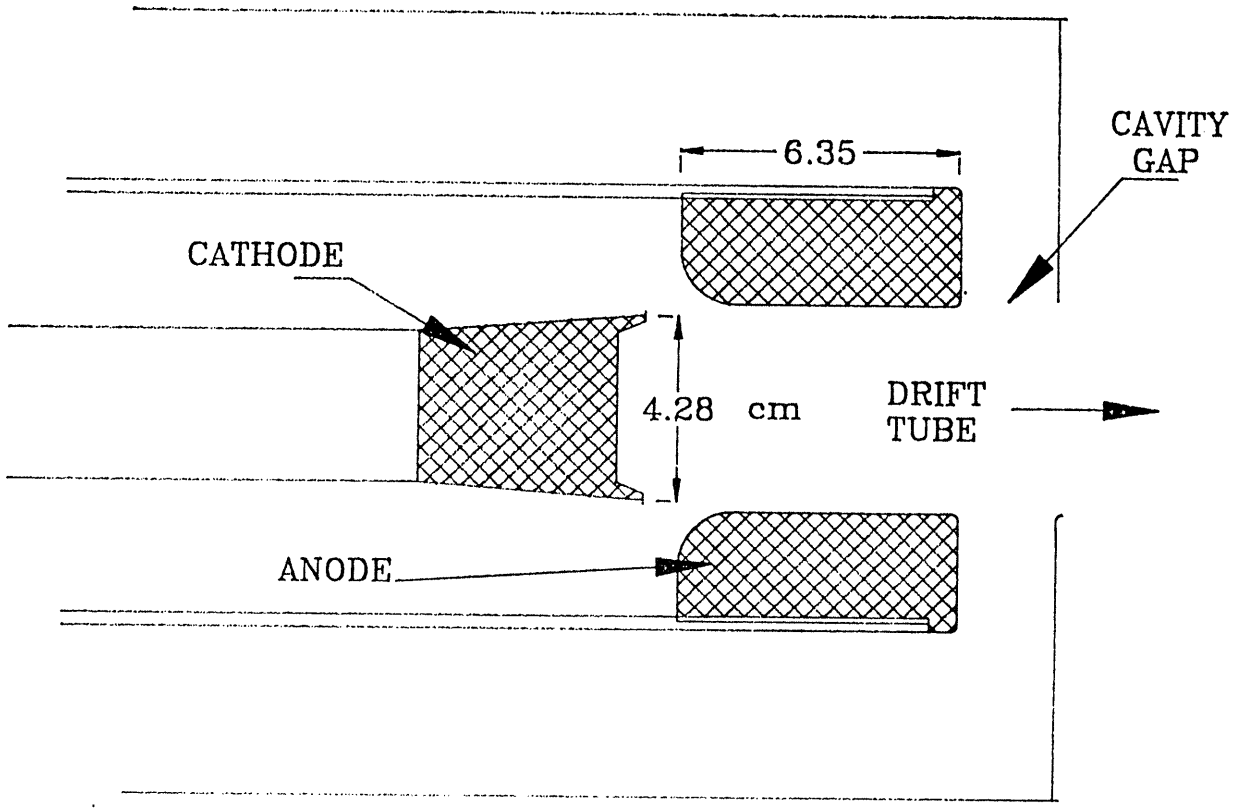

Figure 3. 4 *Diode geometry.*

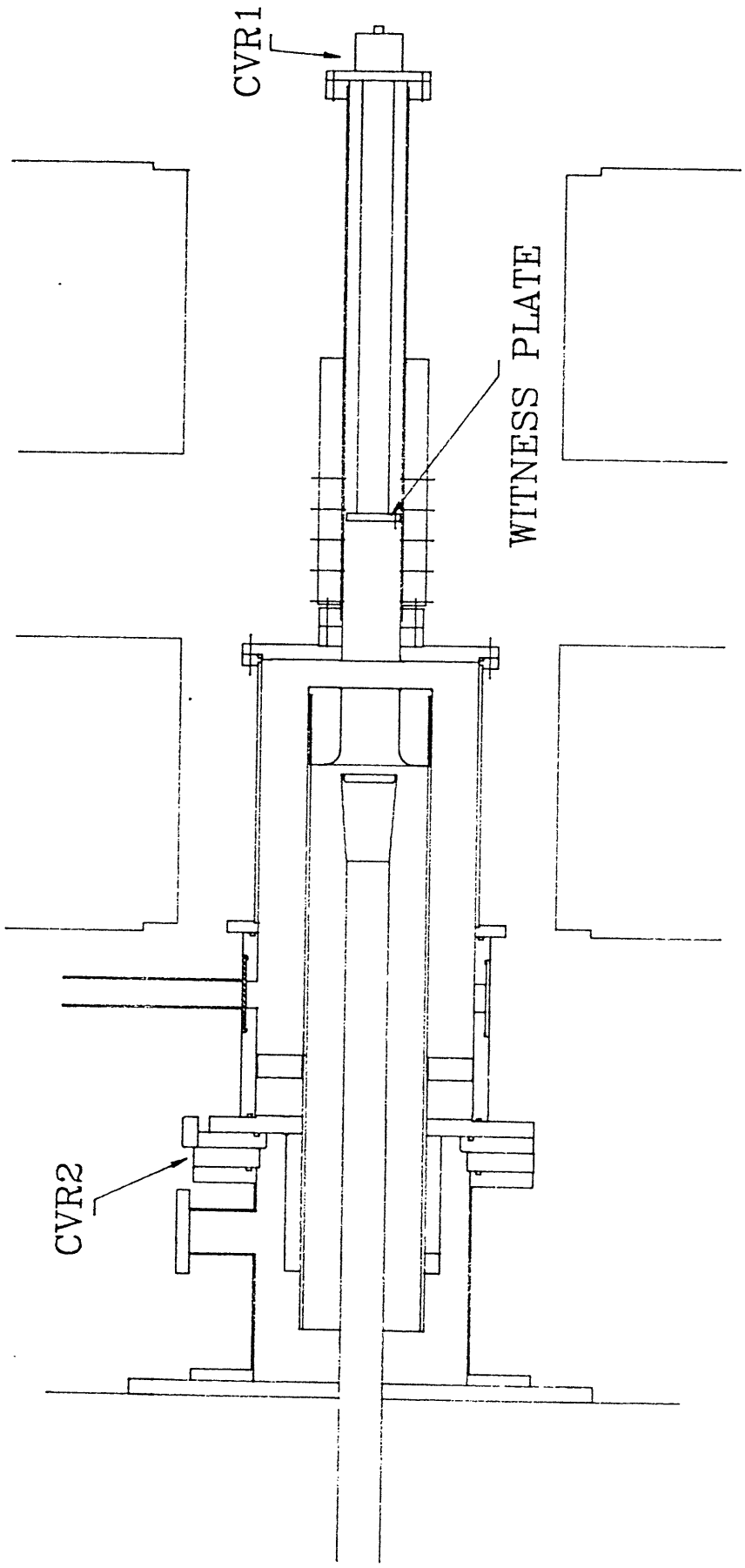

Figure 3. 5 *Current diagnostics.*

into a 40:1 carbon resistor divider and 20 dB coaxial attenuator results in 4 kA/V at the oscilloscope. Unlike CVR1, which can be installed to measure either total or beam current, CVR2 measures total current only.

The amplitude and shape of the total current waveform depend on the diode gap size, Marx charging voltage, main switch design, SF_6 pressure and magnetic field strength. For the optimized diode parameters, total current is 10-12 kA for a diode gap of 1.5 cm. The shown waveform was taken with CVR2 (Figure 3.6). The signal from CVR1, which could not be measured simultaneously, agrees within the shot-to-shot jitter. The diode impedance decreases in time. The time scale on which this occurs is consistent with the phenomenon of gap closure. Plasma formed at the graphite surface slowly traverses the gap, causing the effective gap distance to decrease in time. At 1 cm/μsec, full closure would occur after about 7 pulse lengths. Gap closure effects would tend to be more pronounced at smaller gap distances, also consistent with observation.

DC beam characteristics. Because a substantial portion of the total diode current is intercepted by the anode, beam current cannot be measured by the exact means described in the previous section. Two alternate methods were used. One method made use of the magnetic dipoles which also monitor beam bunching. In order to calibrate the dipoles, the total current was driven through an aluminum shank centered in the drift tube. The integrated magnetic probe signal was compared with the simultaneous measurement of the total current from CVR2 to determine the calibration coefficient. Knowledge of the relative strengths of signals from the five magnetic probes was an added

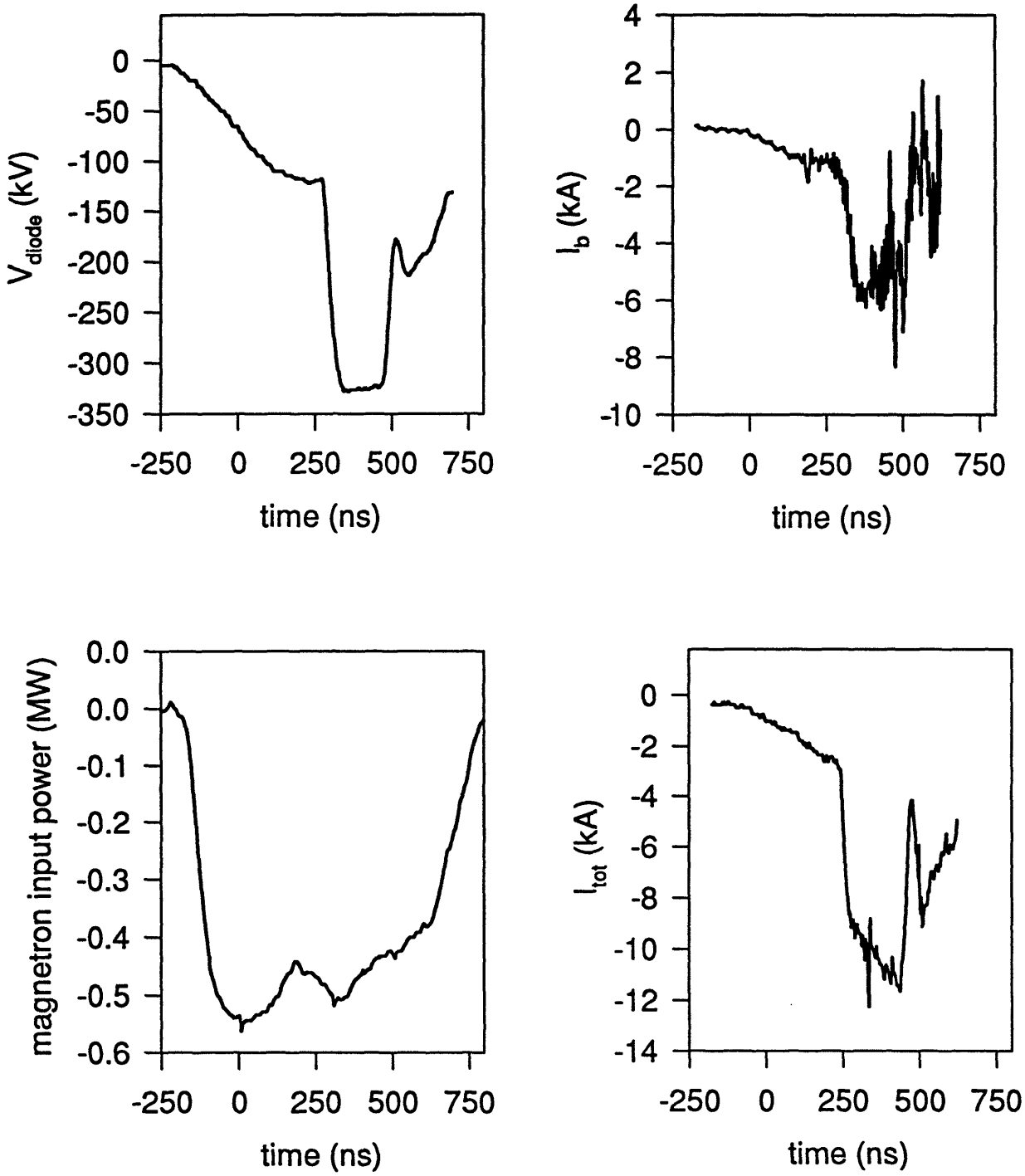

Figure 3. 6 *Nominal diode voltage, magnetron input power, beam current and total current during hot tests.*

side-benefit from these measurements. We also measured beam current with CVR1 and a witness plate positioned at various points along the drift tube. For the nominal diode gap of 1.5 cm, beam currents of about 5 kA were measured with both methods. Results from the magnetic dipole are included in Figure 3.6.

The current measurements with magnetic dipoles were somewhat easier to implement than those with the CVR. The main challenges were to avoid systematic errors during integration or distortion of amplitude due to slow varying noise. To prevent an error due to beam misalignment, the current measurements for 0° and 180° rotations of the drift tube were averaged. With CVR1, difficulties arose which were not an issue in the total current measurements. In order to intercept the beam current, the witness plate diameter must nearly scrape the drift tube wall. Sagging or breakdown can easily shunt the current prematurely to ground. The long shank lengths from CVR to witness plate also complicate the setup. A short, large diameter replacement for the drift tube containing a witness plate and CVR1 could facilitate these measurements in the future.

3.2 Input Cavity

A reentrant cavity configuration was chosen for the input cavity section because of the strong longitudinal gap electric fields of its mode structure. The final cavity design, reached in conjunction with extensive MAGIC simulations, is notable for its compactness, simple power coupling and tunability (Figure 3.7, Figure 3.8). The compactness is achieved by consolidating the diode and input cavity, which reduces the system length and eases requirements on the guide magnetic field. Power is injected into the cavity radially

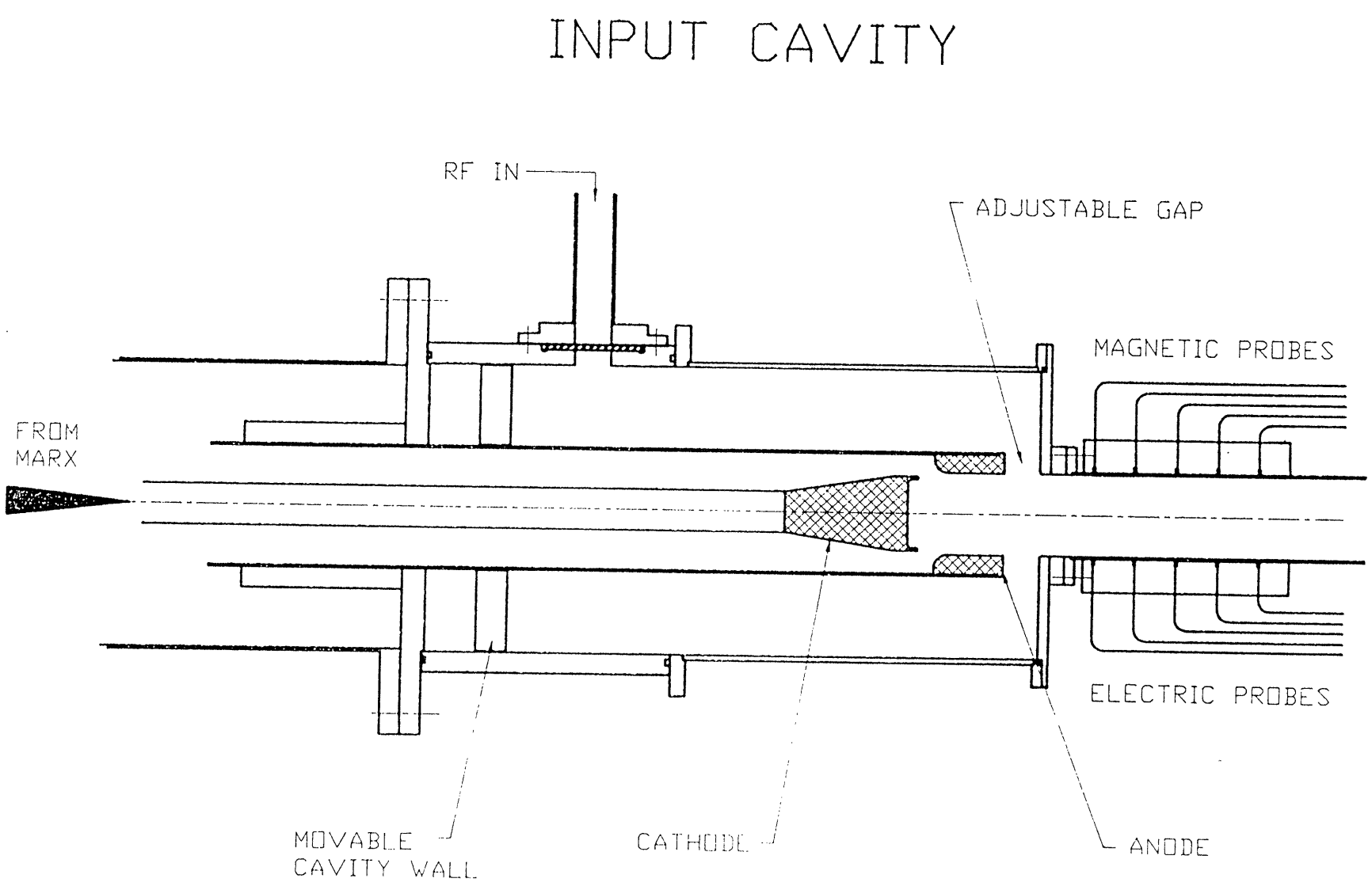

Figure 3. 7 *Experimental Set-up I: input cavity, electron gun, drift tube, and current modulation diagnostics.*

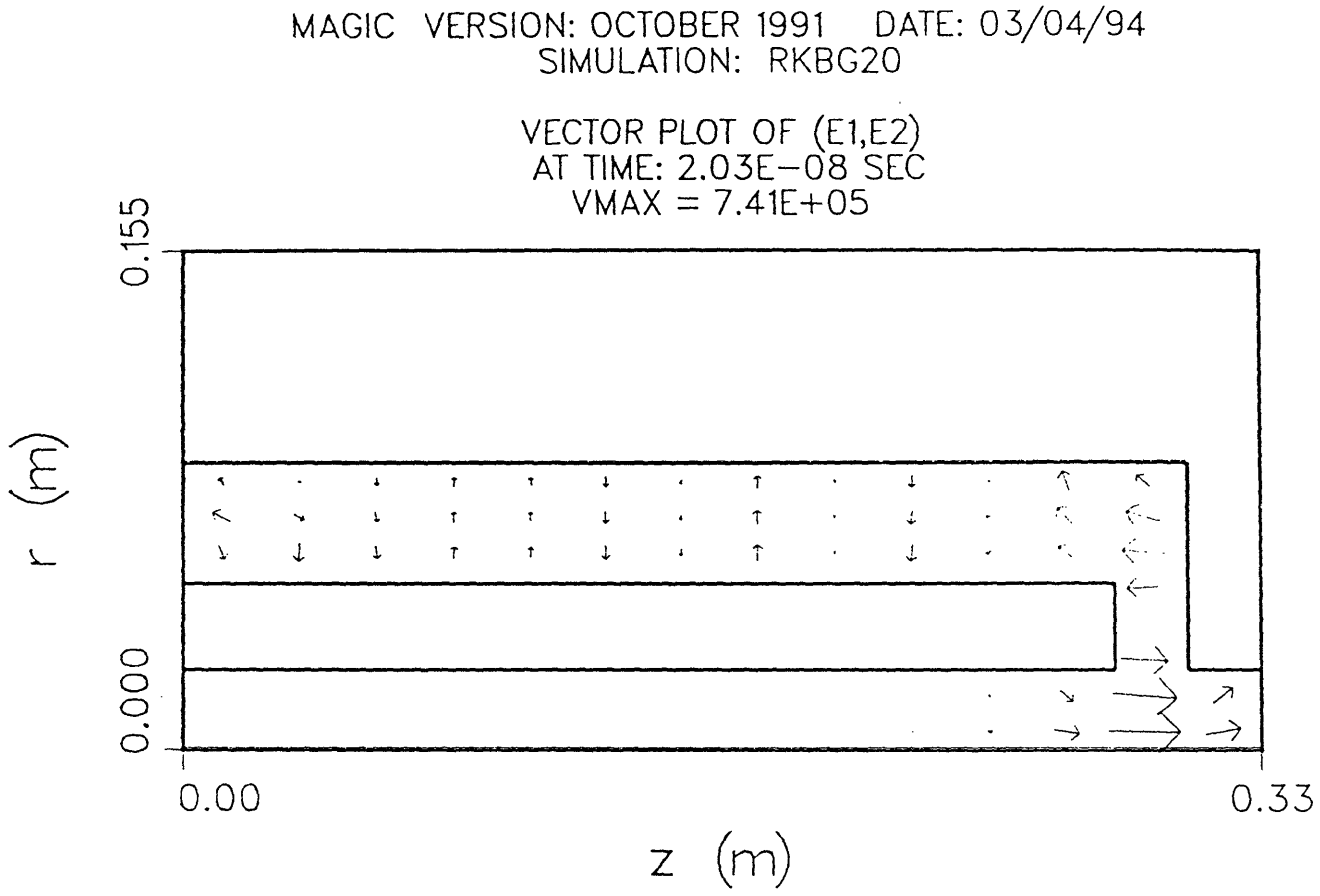

Figure 3. 8 *Vector plot of electric field strength inside the input cavity. The antenna, which excites the radial electric field, is located a quarter wavelength from the left end of the cavity, near the outer wall. There is no beam loading.*

from a single C-band waveguide. The rectangular input port is oriented so that the H field of the TE_{10} mode couples to the H_ϕ field in the cavity and is positioned one quarter wavelength from the cavity wall. There is no power splitting, phase adjustment or extra twists to complicate the structure. Five adjustable stub tuners inset into the cavity wall are available just in case a good azimuthally symmetric mode could not be achieved. The five tuner ports plus input port are equally spaced around the cavity perimeter.

Other tuning knobs are incorporated into the cavity design. The nominal cavity length of 7/2 the free space wavelength (8.9 cm) can be adjusted by $\pm\lambda/4$. Fine adjustments in both back flange position and orientation with respect to the walls are possible. The lip of the reentrant cavity is formed by a graphite plug facing the end flange and can be varied from 0 to 1 inch as shown in Figure 3.7. It is the opposite end of this graphite plug which serves as anode in the electron gun. These features, combined with the tunable input source, provide the basis for empirical optimization of the cavity.

The cavity, drift tube, diode and diode insulating structure are evacuated to pressures in the low 10^{-5} Torr by a Leypold turbo pump. A quartz window provides the interface between the evacuated cavity and the microwave input plumbing between the magnetron and the window, which is pressurized with SF_6 gas.

3.3 RF Source

The RF input source is a 1 MW, 0.5 μsec magnetron operating in the frequency range of 3.1-3.5 GHz. The output frequency can be tuned to a fraction of a MHz. The

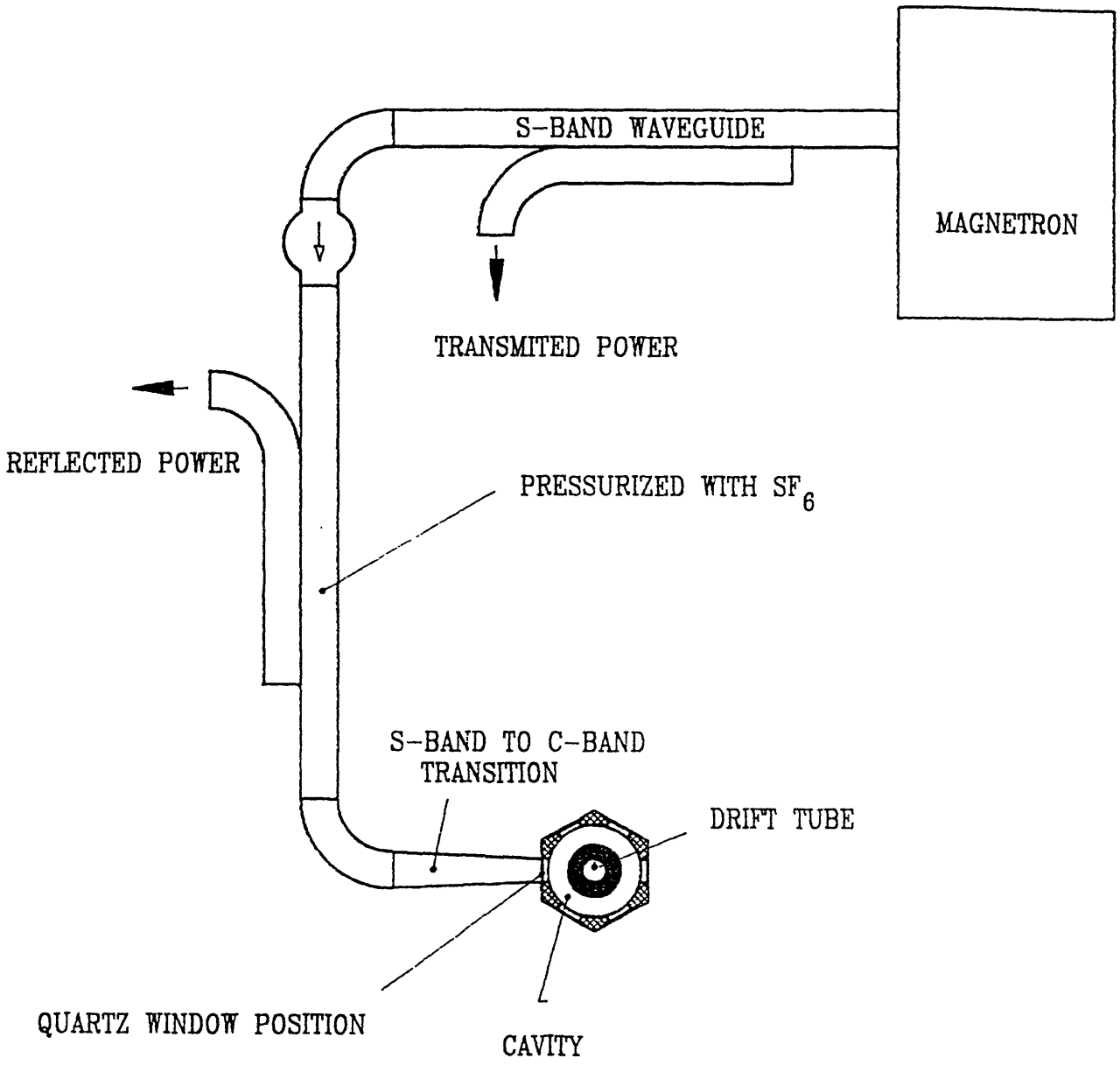

Figure 3. 9 *Experimental Set-up II: RF injection to input cavity and diagnostics.*

magnetron, a Hercules unit, was built in 1958 at Bell Labs, but later substantially modified. Figure 3.6 includes a typical magnetron output pulse.

The plumbing connecting the magnetron to the cavity is shown in Figure 3.9. Directional couplers are used to monitor incident and reflected power of the cavity. The ferrite isolator inbetween the two couplers ensures that the incident power measurements are not contaminated in case of high reflection. One of the challenges in installing the plumbing was mechanical. Both the magnetron and the Marx-PFL-cavity structure are unyieldingly rigid. Slight twists and misalignment in the plumbing placed sufficient strain on the waveguide joints to cause damage. Thus, two flexible waveguides form part of the structure. When the structure is pressurized to 11 psi SF_6, it can handle at least 0.5 MW power without breakdown.

The magnetron lower output level threshold is about 100 kW. In order to perform measurements in the range below 100 kW, a 20 dB directional coupler from which power is tapped is inserted after the first directional coupler (refer to Figure 3.9). It is followed by a variable attenuator and an additional directional coupler to monitor incident power. This setup was used to benchmark bunching at intermediate input power levels.

3.4 Drift region and guide magnetic field.

Following the cavity gap, the beam enters a drift region constructed of a two foot long stainless steel cylindrical pipe. With a diameter of 4.75 cm, the drift tube is cutoff at 3.7 GHz for the fundamental TE_{11} vacuum mode and 4.8 GHz for the TM_{01} mode. A

graphite collector terminates the drift tube, although most of the beam hits the walls before reaching the collector as it follows the magnetic field line.

Beam confinement is established by a superconducting magnet manufactured by Cryomagnetics, Inc.. Field strengths of up to nearly 20 kG are possible. The magnet coil consists of a double-Helmholtz pair. The 1% uniform field extends for 10 cm length and 3% uniformity exists for 20 cm length (Figure 3.10). The gap and diagnostics are all within the uniform field, while the diode was located in the linear region of the field.

Beam alignment was assessed by placing a witness plate covered with thermal paper at various locations in the drift tube. Examples of damage patterns are shown in Figure 3.11. From these we see that the beam radius is about 1.9 cm and the beam thickness is at most 0.3 cm.

3.5 Bunching Diagnostics

An array of electric and magnetic dipoles line the drift tube to measure bunching levels downstream from the cavity gap. The dipoles are constructed from 0.141 inch semirigid coax, and are slightly inset from the drift tube inner surface (about 0.2 mm). Five probes of each type positioned diametrically opposite each other cover axial distance from 2.3 to 6.3 inches from the center of the cavity gap. The probe signals are transmitted to the screen room by equal lengths of 0.5" semi-rigid cable. The attenuation at 3.3 GHz of each of these cables is about 2 dB. Inside the screen room the signals are bandpass filtered, rectified with calibrated crystals and then sent to the oscilloscope.

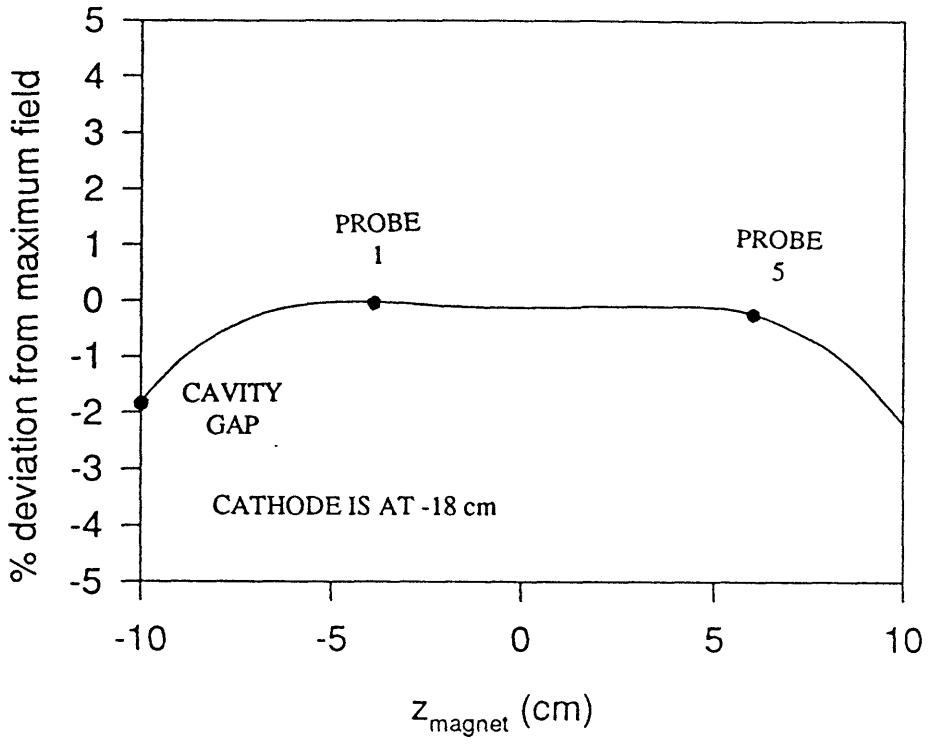

Figure 3. 10 *Superconducting magnet guide field uniformity along axis.*

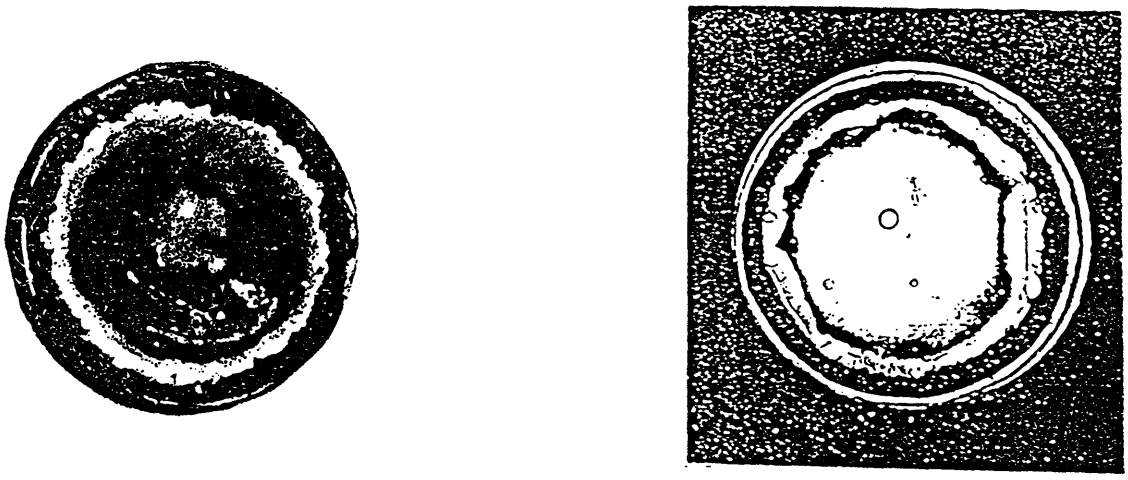

Figure 3. 11 *Thermal paper damage patterns measured inside drift tube during beam alignment measurements.*

The probes are calibrated with a traveling TM_{01} wave of known power, using the setup shown in Figure 3.12. RF from a CW source passes through a TE_{11} rectangular to TM_{01} circular mode converter. The wave then passes through the section of drift tube used in the experiment and a standing wave meter terminated with a matched load. Since the input power is known, the field strengths at the cavity wall can be computed, as well as the ratio of the probe signal to those fields: $P_{probe}=K_E|E_{r1}|^2$, $P_{probe}=K_B|B_{\theta 1}|^2$, where K_E and K_B are the coupling constants. Once this calibration factor is known, relations to be derived in the first section of Chapter Four can be used to determine the current modulation level from dipole probe measurements during experiments.

This set-up has the significant advantage of allowing calibrations to be performed *in situ*, albeit at a frequency above the RKA operating frequency. The cutoff frequency of the TM_{01} vacuum mode in the drift tube is 4.8 GHz, and is set by the design requirement that the fundamental TE_{11} mode at 3.3 GHz not be able to propagate. The calibrations take place at 5.15 GHz. The frequency-dependent evanescent decay length is not an important effect in the calibration factor. The probes are only inset 2 mm from the drift tube wall and are small compared with the e-folding length.

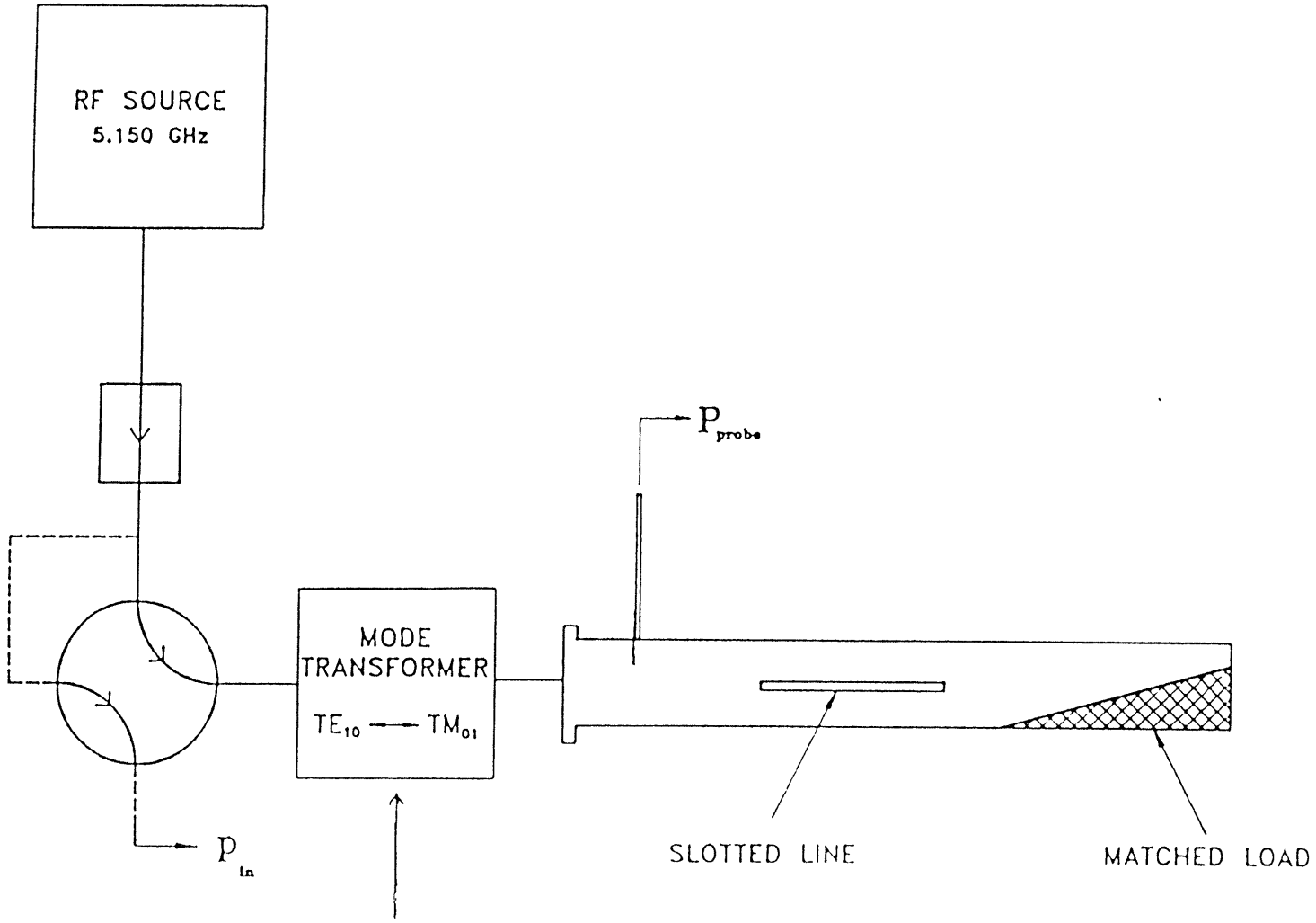

Figure 3. 12 *Calibration set-up for current modulation probes.*

CHAPTER FOUR

Experimental results and comparison with theory

4.1 Relation of RF magnetic and electric field at the wall to current modulation.

4.1.1 Magnetic field relations.

The relations between the RF magnetic and electric field and the current modulation are required in order to calculate the value of percent bunching from the probe diagnostics used in the experiment as illustrated schematically in Figure 4.1. The signals from the magnetic and electric probes are proportional to the amplitude of the total RF field, which contains a contribution from each space charge wave. In the small signal regime, for the time varying component of current of the slow I_{1s} and fast I_{1f} space charge waves:

$$I_1 = I_{1s}e^{-jk_s z} - I_{1f}e^{-jk_f z}$$

the magnetic field at the wall for the TM_{01} mode is found from Maxwell's equations to equal:

$$B_1 = \frac{\mu_0}{2\pi b}\left(\frac{I_{1s}}{\kappa_s}e^{-jk_s z} - \frac{I_{1f}}{\kappa_f}e^{-jk_f z}\right)$$

where κ_s and κ_f are functions of k_z and ω which reduce to unity for long wavelengths:

$$\kappa_s = \frac{I_0(p_s b)}{I_0(p_s a)} \text{ and } \kappa_f = \frac{I_0(p_f b)}{I_0(p_f a)}$$

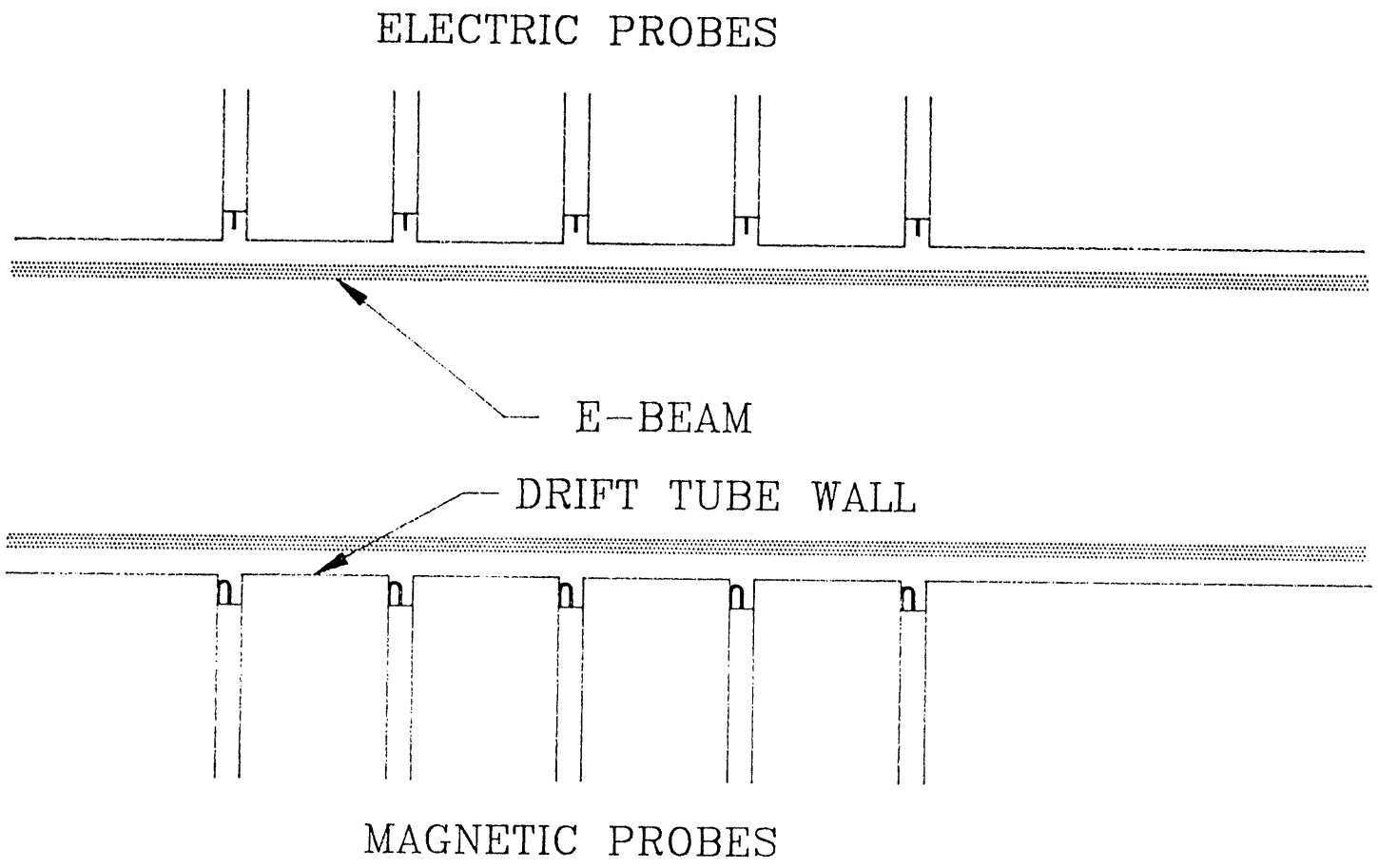

Figure 4. 1 *Current modulation diagnostics - detail.*

with $p^2 = k^2-(\omega/c)^2$. The shorthand $k_z=k$ will be used. At the first maximum of the current modulation envelope, z = 9 cm, the magnetic field amplitude is proportional to a weighted sum of the fast and slow current waves:

$$\left|B_{\theta 1}(\frac{\lambda_{rel}}{4})\right| = \frac{\mu_0}{2\pi b}(\frac{I_{1s}}{\kappa_s}+\frac{I_{1f}}{\kappa_f})$$

4.1.2 Electric field relations.

The TM_{01} small signal component of E_r can be computed from B_θ for each space charge wave, that is,

$$E_{r1} = \frac{c^2 k}{\omega} B_{\theta 1}.$$

Combining the slow and fast space charge wave contributions

$$E_{r1}(z) = \frac{1}{2\pi\varepsilon_0 b}\frac{1}{\omega}(k_s \frac{I_{1s}}{\kappa_s}e^{-jk_s z} - k_f \frac{I_{1f}}{\kappa_f}e^{-jk_f z})$$

yields the electric field amplitude:

$$\left|E_{r1}(\frac{\lambda_{rel}}{4})\right| = \frac{1}{2\pi\varepsilon_0 b}\frac{1}{\omega}(k_s \frac{I_{1s}}{\kappa_s} + k_f \frac{I_{1f}}{\kappa_f}).$$

In the long wavelength limit, if $I_{1s}\sim I_{1f}$, the electric field is proportional to the mean wavenumber.

$$\left|E_{r1}(\frac{\lambda_{rel}}{4})\right| = \frac{1}{2\pi\varepsilon_0 b}\frac{k_{mean}}{\omega}\left|I_1(\frac{\lambda_{rel}}{4})\right|$$

$$= \frac{1}{2\pi\varepsilon_0 b}\frac{1}{v(1-\frac{\varepsilon}{\beta^2})}\left|I_1(\frac{\lambda_{rel}}{4})\right|$$

Because of the dispersion in the drift tube, the velocity modulation amplitudes of the fast and slow waves are not necessarily equal, even if the current modulation components are excited with equal amplitude. Thus, although the total velocity modulation amplitude is minimum at $\lambda_{rel}/4$, it is not necessarily zero. For $\varepsilon << \beta^2$, however, k_s and k_f are almost identical, and the difference between v_{1s} and v_{1f} is small. In this case, at the beat maximum, $I_1 = \lambda_1 v_0 + \lambda_0 v_1$ becomes:

$$|I_1| \approx |\lambda_1| v_0$$

For this special case, the electric field reduces to the familiar quasi-static limit:

$$|E_1| = \frac{|\lambda_1|}{2\pi\varepsilon_0 b}$$

Axial dependence of fields. The above results for E_r and B_θ are applicable at the space charge modulation maximum. The general z-dependent expressions for the field magnitudes are:

$$|B_{\theta 1}(z)| = \frac{\mu_0}{2\pi b}\sqrt{\left(\frac{I_{1s}}{\kappa_s} - \frac{I_{1f}}{\kappa_f}\right)^2 + 4\frac{I_{1s}I_{1f}}{\kappa_s\kappa_f}\sin^2(k_{rel}z)}$$

$$|E_{r1}(z)| = \frac{1}{2\pi\varepsilon_0 b}\sqrt{\left(\frac{k_s}{\omega}\frac{I_{1s}}{\kappa_s} - \frac{k_f}{\omega}\frac{I_{1f}}{\kappa_f}\right)^2 + 4\frac{k_s k_f}{\omega^2}\frac{I_{1s}I_{1f}}{\kappa_s\kappa_f}\sin^2(k_{rel}z)}$$

In the long wavelength limit, κ_s and κ_f approach unity and the magnetic field is related to the current at any axial position z by the well-known quasistatic result:

$$|B_{\theta 1}(z)| = \frac{\mu_0}{2\pi b}|I_1(z)|$$

Note that $I_1 = I_{1s}e^{-jk_s z} - I_{1f}e^{-jk_f z}$. With the additional restriction $I_{1s} \sim I_{1f} = I_{1s,f}$, the electric field can be written:

$$|E_{r1}(z)| = \frac{1}{2\pi\varepsilon_0 b}(2I_{1s,f})\sqrt{(\frac{k_{rel}}{\omega})^2 + \frac{k_s k_f}{\omega^2}\sin^2(k_{rel}z)}$$

where $k_{rel} = (k_s - k_f)/2$. Factors of k_f and k_s weight the fast and slow components of E_{r1}, while the fast and slow components of $B_{\theta 1}$ reduce separately to non-dispersive expressions. The relative simplicity of expressions for magnetic field compared to electric is a consequence of TM mode structure.

4.1.3 Range of validity study

For realistic experimental parameters, it is possible to push the RKA operating regime away from the long wavelength limit. In this case, it may be necessary to include κ_s and κ_f in the proportionality constants. Correction factors to the long wavelength constants as high as 40% have been cited in the literature [Lau, 1989]. These computations assume that $I_{1s} \sim I_{1f}$, so that the correction to the magnetic field constant is $2\kappa_s\kappa_f/(\kappa_s+\kappa_f)$. However, if the assumption on current amplitudes were violated, the correction factor could be overestimated by the preceeding expression. Moreover, differing current amplitudes become more likely as the correction factor $2\kappa_s\kappa_f/(\kappa_s+\kappa_f)$ increases. We determined the range of validity for our geometry by comparing proportionality constants between the fields and currents extracted from MAGIC simulations to those calculated from the analytic expressions.

Simulations. Design simulations were performed using MAGIC, a 2 1/2-d PIC code developed by Mission Research Corporation. MAGIC solves the full Maxwell equations in conjunction with the Lorentz force equation to obtain self consistent solutions for electromagnetic fields and charged particle trajectories. Given a cylindrically symmetric geometry, MAGIC treats electromagnetic fields as functions of r and z and can account for 3-d motion of particles. Asymmetries such as the single-sided power injection are not modelled by the simulation [Goplen, 1991]. Benchmark simulations of experimental results from the NRL 1.3 Ghz RKA, performed by Dr. C. Chen, confirmed that MAGIC is an appropriate code for RKA modelling.

Simulations of the input cavity section were run with various beam currents and radii. Current and field diagnostics were placed at the modulation envelope maximum particular to each case. Final runs were done with twenty particles emitted per timestep to reduce noise due to discrete particle effects. The amplitude of the field and current modulation was determined by applying curve fits at one or more points of time. Output from a typical simulation is included in Figure 4.2. Attempts to increase κ_s and κ_f by simply increasing I/I_L were foiled by MAGIC, as the simulations failed at I/I_L not much higher than 0.53. Note that I_L used in the ratio is appropriate for a smooth, uninterrupted drift tube and does not include the significant reduction of limiting current in the presence of the cavity gap.

The analytic theory is compared to simulation in Figure 4.3. For small correction factors, agreement is good. Deviation starts near a correction factor of 1.2 and becomes increasingly significant for higher correction factors. The trends shown in the simulations

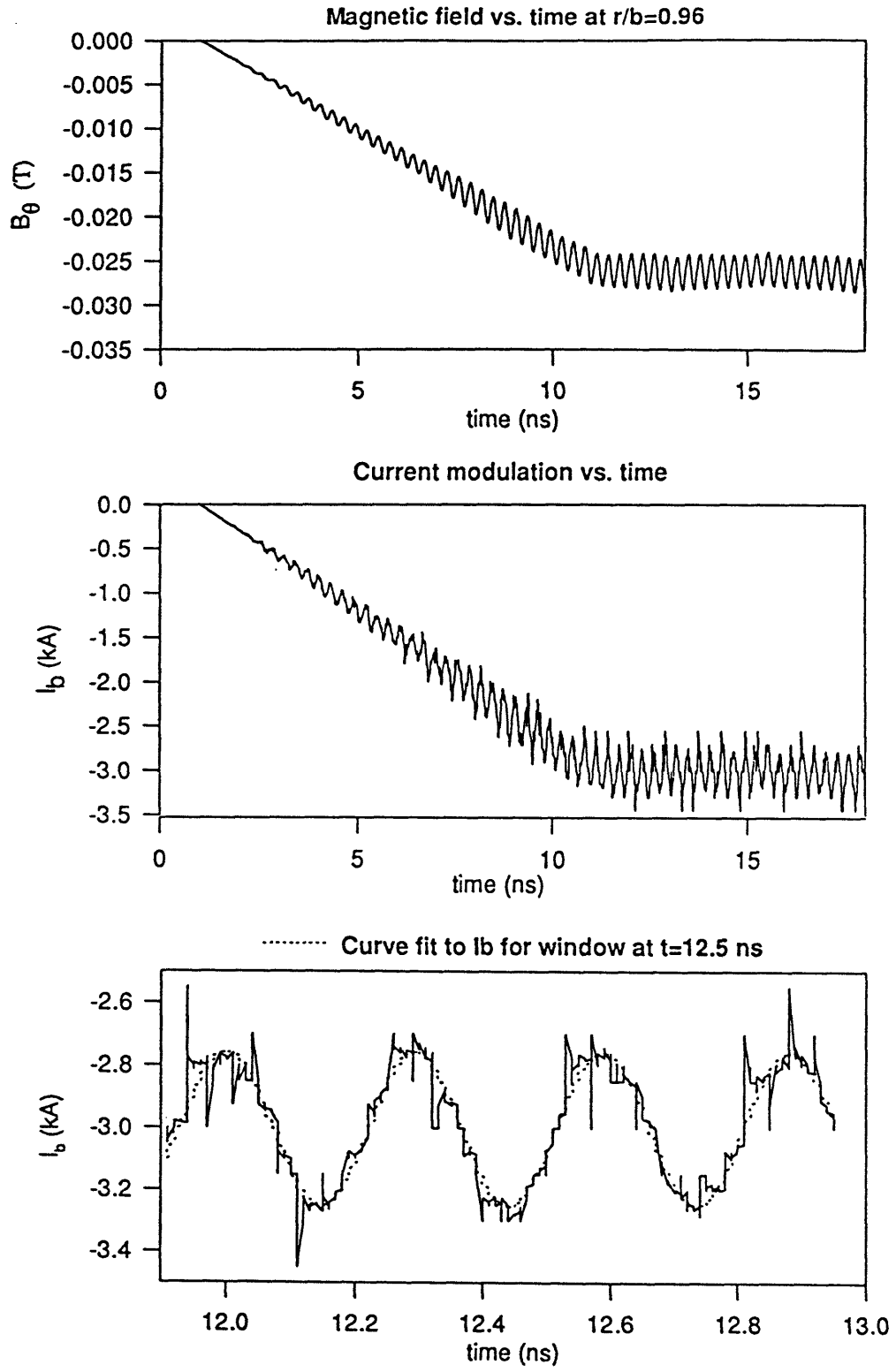

Figure 4. 2 *Output from simulation used to compute $|I_1/B_{\theta 1}|$ at $\lambda_{rel}/4$. Parameters: I=3kA, I/I_L=0.29, a=1.89cm, b=2.35cm, z=13.75cm, f=3.4GHz.*

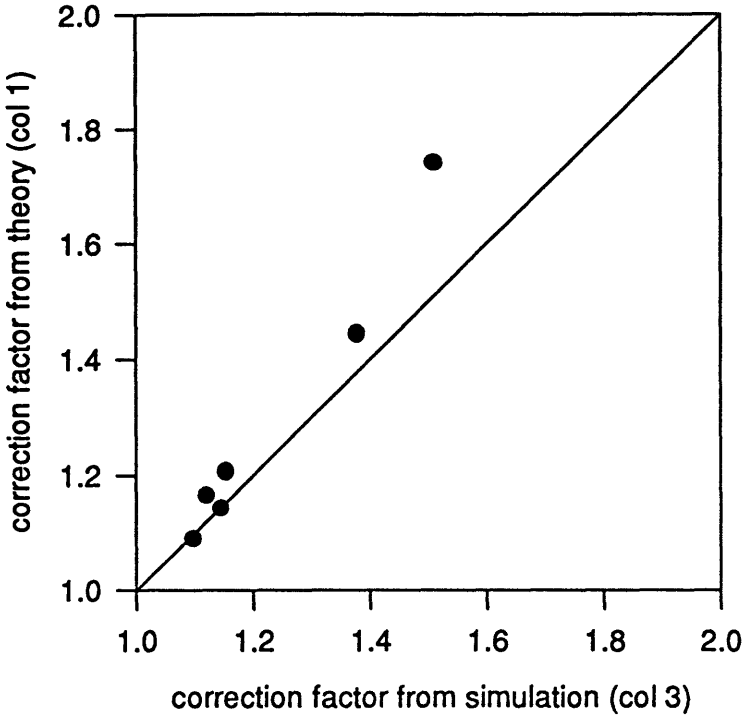

-------CORRECTION FACTOR:------- -------PARAMETERS:-------

$\frac{2\kappa_f\kappa_s}{\kappa_f+\kappa_s}$	$\frac{2\kappa_f\kappa_s}{\kappa_f+\kappa_s}$ (long λ)	Simul'n	I (kA)	$\frac{I}{I_c}$	a (cm) (b = 2.35 cm)
1.090	1.092	1.098	5.5	0.28	2.095
1.143	1.149	1.145	5.5	0.40	1.990
1.166	1.172	1.120	3.0	0.29	1.890
1.207	1.223	1.153	5.5	0.53	1.890
1.741	1.809	1.51	0.83	0.50	0.1533

Figure 4. 3 *Calculated current modulation correction factors:* $|I_1/B_{\theta 1}|=(2\pi b/\mu_0)$x(correction). *Analytic theory for* $I_{s1} \approx I_{f1}$ (correction = $2\kappa_s\kappa_f/(\kappa_s+\kappa_f)$) *is compared to simulation results in the table and plot above. Column 1 of the table is plotted against Column 3. The computation for Column 1 uses* k_s *and* k_f *which are solutions to the full dispersion relation. In Column 2,* k_s *and* k_f *are approximated from the long wavelength dispersion relation.*

can be interpreted in terms of gap effects at short wavelengths. As $2\kappa_s\kappa_f/(\kappa_s+\kappa_f)$ increases, the separation between k_f and k_s increases, and λ_s, which is the smaller of the two space charge wavelengths, can become comparable to the gap distance. Transit time effects then reduce the efficiency of excitation of this wave compared to the fast wave and $I_{1s} \sim I_{1f}$ becomes a poor approximation. The correlation of the deviation between simulation and theory with λ_s supports this argument (Figure 4.4). The error is a few percent for gaps of about $\lambda_s/2$ and 15% for gaps about equal to λ_s.

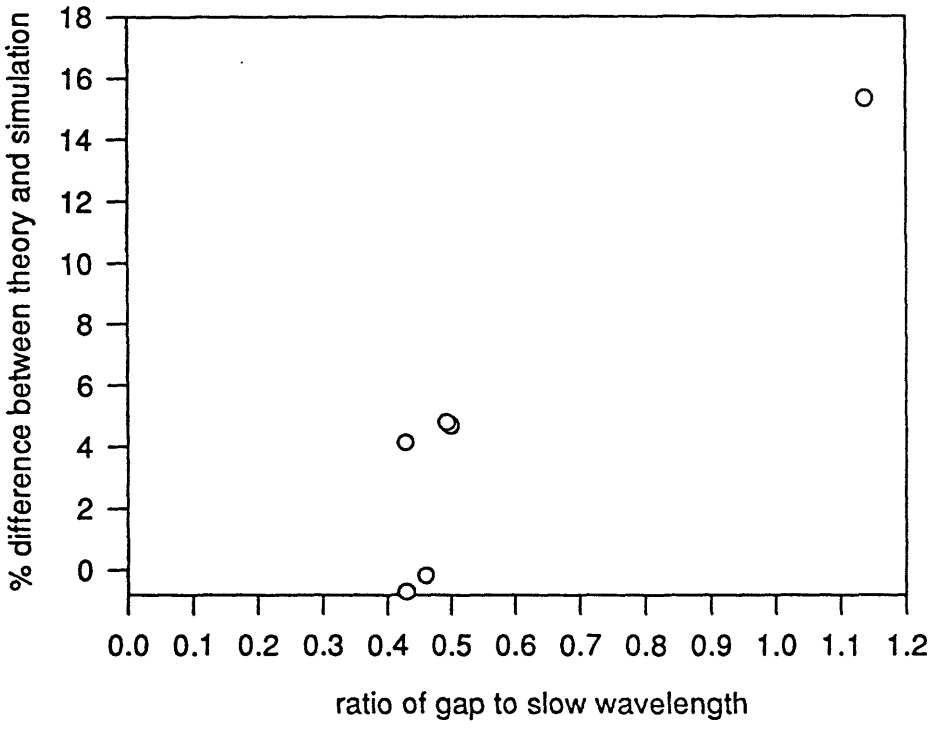

Figure 4. 4 *Correlation of discrepancy between simulation and theory of the current modulation correction factor with the ratio of cavity gap length to* λ_s.

4.2 Cold tests on the cavity.

The purpose of the cold tests in the absence of the electron beam is to tune the cavity to an appropriate operating mode. Criteria for the operating mode are that the E_z field at the position of the beam be uniform in azimuthal angle θ, and that the frequency not be close to the upper and lower limits of the magnetron range. If the cold resonance is too low or high, beam loading may cause the original resonant frequency to shift outside the magnetron range. Because cold tests can be done with a C-W source, the characteristic modes in the vicinity of the operating mode can be studied in a reasonable length of time. Under pulsed, loaded conditions such a survey would require considerable time and effort.

Microwave radiation of tens of mW is provided by the CW source, whose output frequency is tracked by a frequency counter. A 3 dB coupler is included in the plumbing to monitor reflected power from the cavity (Figure 4.5). Field strengths inside the cavity are measured with an electric dipole which couples to E_z at the beam radius. The probe can be rotated around the axis of symmetry to plot out the angular dependence of the field at the beam position.

A thorough scan of the cavity response over the parameter space was performed. For each cavity length, frequency was varied from 3.1 to 3.5 GHz, and resonances and azimuthal mode numbers were recorded. Results are plotted in Figure 4.6, below MAGIC results. The variation in strength of coupling with the cavity length was found to peak when the distance between the cavity end and input waveguide port is about $\lambda/2$, a reasonable result since incident power from the RF source couples to the H_θ field which

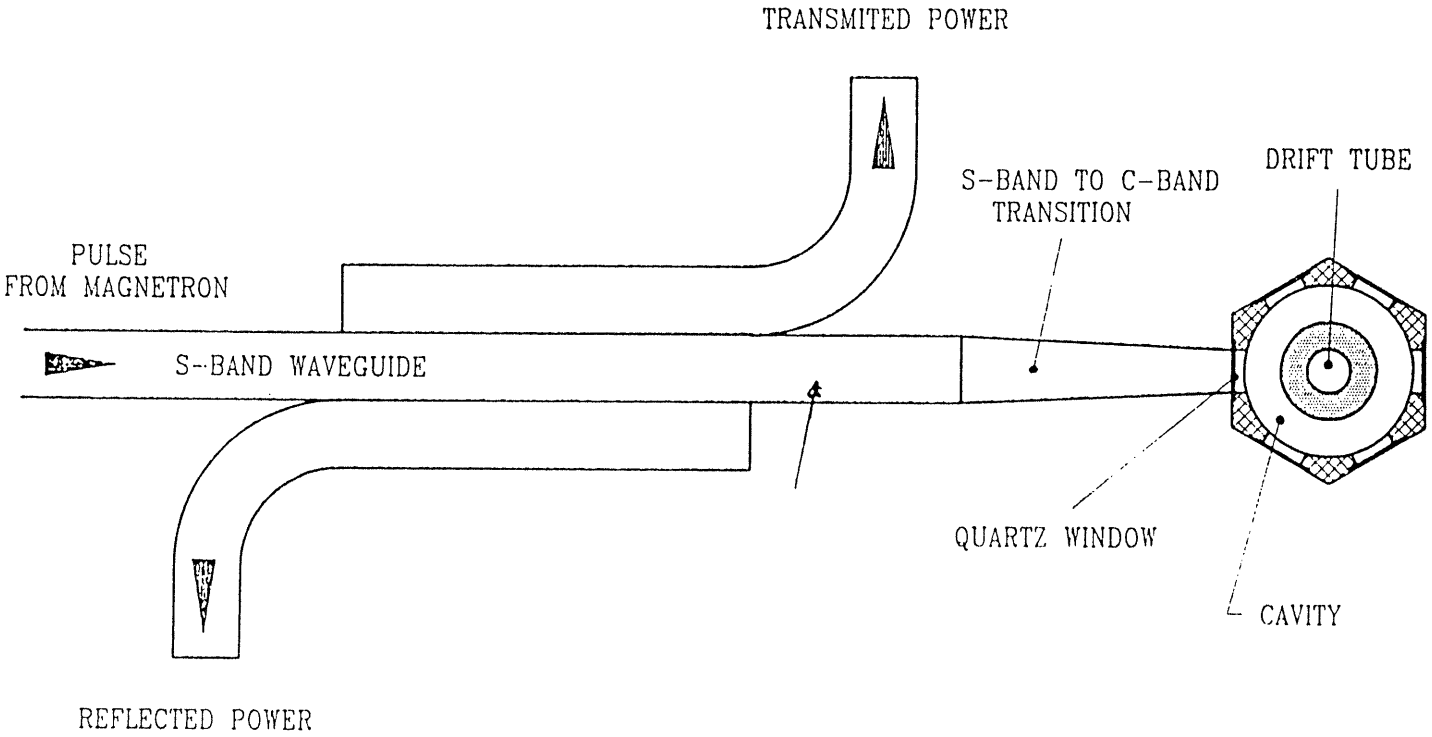

Figure 4. 5 *Cold test set-up.*

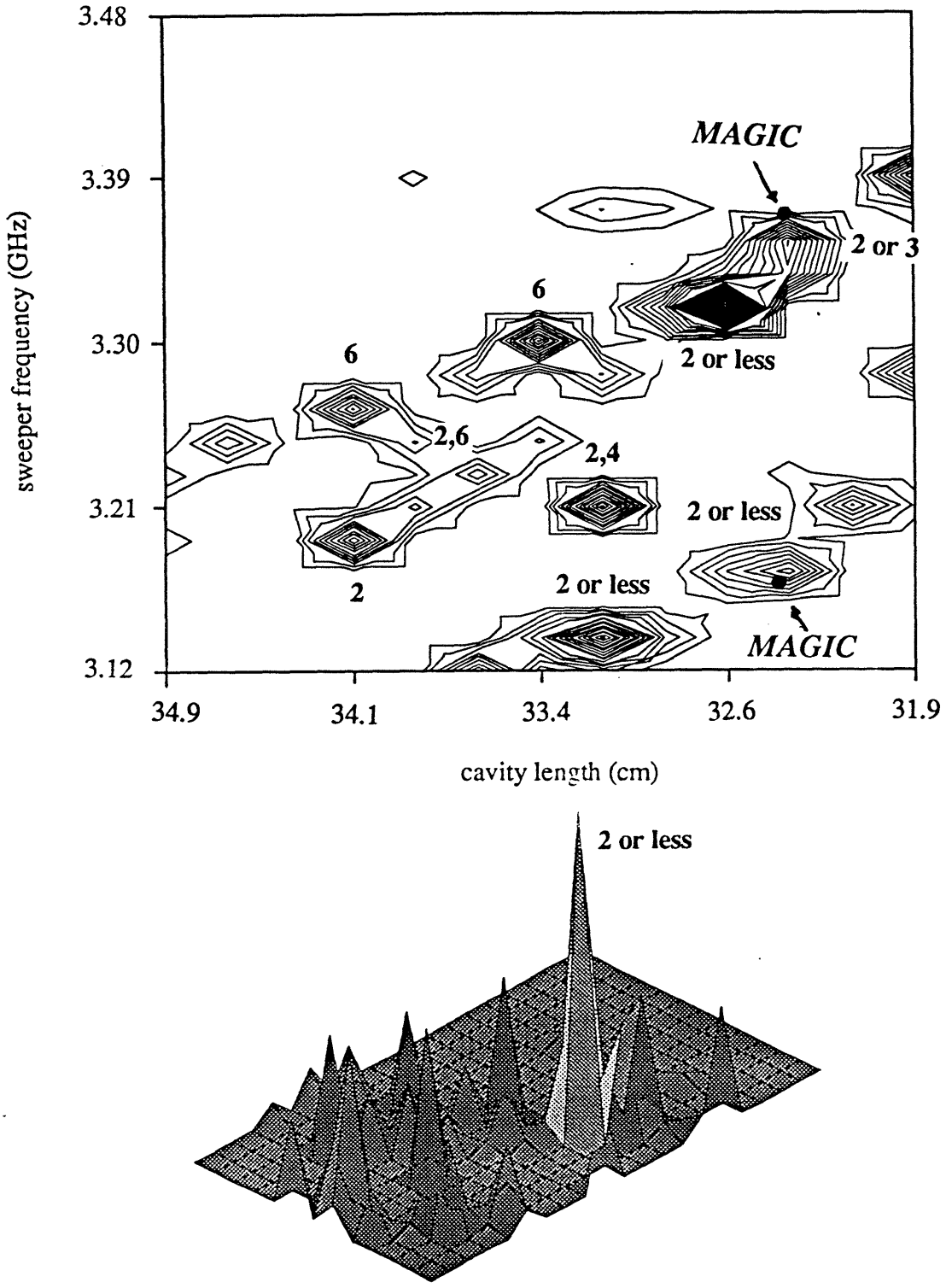

Figure 4. 6 *Contour plot of cavity resonant frequencies measured during cold tests as a function of cavity length and frequency, before tuning. Some peaks are labelled with the number of maxima observed in a full rotation in* θ. *Resonances predicted by MAGIC simulations for the nominal cavity length of 32.2 cm are marked.*

has a maximum at that point. It was found that the two modes of lowest azimuthal mode number were tunable to uniformity. The success in achieving the uniform mode without the added complexity of the tuners is particularly satisfying. The resonance at 3.383 GHz was chosen as operating mode. It was possible to tune this mode to within 96% uniformity in electric field by adjusting the position of the back flange (Figure 4.7). Frequency response was also recorded, yielding a cold Q of about 370. Uniformities of 85% in amplitude can be obtained and maintained with reasonable effort and were used for first studies of beam bunching.

4.3 Cavity Hot-tests - Current modulation studies

The tuned cavity was returned to the accelerator for high power tests with the beam. Current modulation was observed and its dependence on input power, axial position, guide field and diode gap was studied. Cavity response under loaded conditions was also determined and attempts were made to optimize coupling of incident power. In each of the following sections, measurements as a function of one parameter are described and compared with theory and simulation.

4.3.1 Bunching dependence on input power.

Input power scaling provides an simple and effective test of bunching behavior. For small signals and negligible gap transit times, current modulation should scale linearly with gap voltage ($\sim E_z$), which is proportional to the square root of input power. Plotted

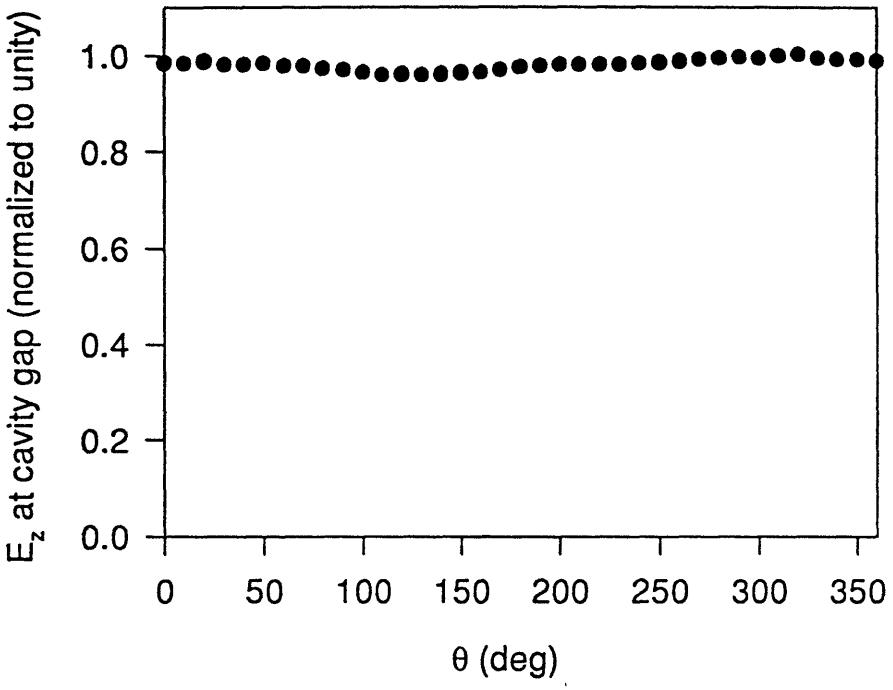

Figure 4. 7 *Results of empirical optimization of cavity under unloaded conditions (i.e no beam.) Normalized longitudinal electric field strength at the beam position is plotted against azimuthal angle* θ.

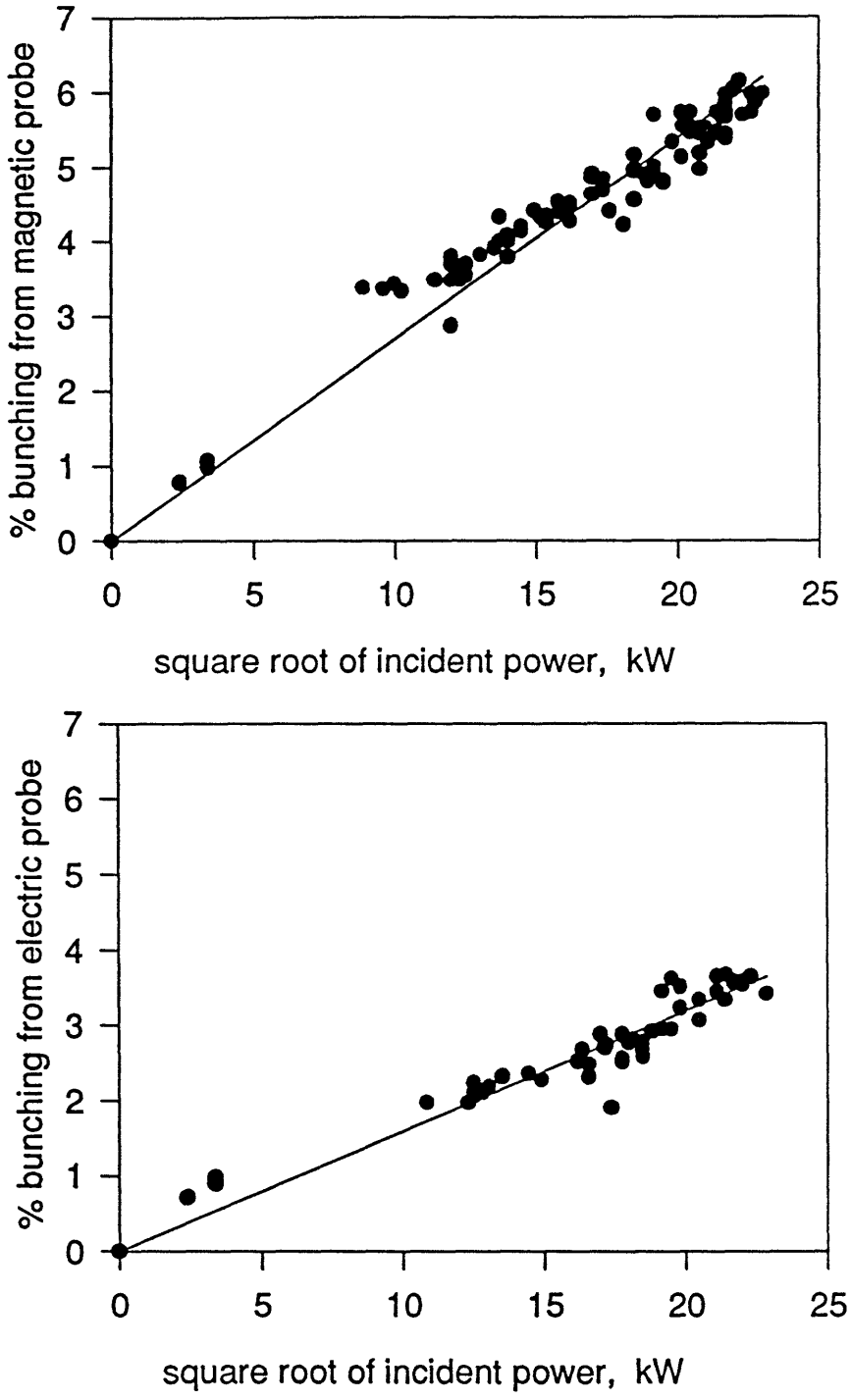

Figure 4. 8 *Scaling of beam bunching with input power.* V_{ch}*=350kV, B=10kG, I=5kA.*

in Figure 4.8, the experimental results exhibit the expected linear dependence. MAGIC simulations also confirm the simple scaling. The data also provides information on the reliability of the two types of dipole probes. Placing diagnostics in the hostile environment near the inner drift tube wall could potentially cause problems such as charging up or breakdown at the probes. The data from the electric and magnetic probes, which are both situated at z=11 cm, is similar, implying that their ability to yield accurate results for these experiments is comparable.

The magnetic probes reach up to 6% current modulation for 500 kW input power, while the electric probes show about 3% modulation. These figures, as well as all other experimental results in this thesis, are based on the long wavelength relations derived in the first section of this Chapter. These relations provide a conservative estimate of the bunching level. For example, the correction factor found from simulations of our experimental set-up for the magnetic dipoles is 1.15 (Figure 4.3), which would correspond about 7% bunching at 500 kW. For electric probes, the correction factor, which is about 1.25, corresponds to over 4% bunching.

4.3.2 Bunching dependence on axial position, guide magnetic field, and beam current.

Measurements of bunching dependence on axial position and beam current provide important design information and a means to test the theoretical predictions for the spatial characteristics of the current modulation. Bunching dependence on z was determined by recording simultaneous probe outputs at four different axial positions separated by 2.5 cm

along the z axis. Figure 4.9 shows the time traces from such a shot. The 200 ns wide signals coincide temporally with the beam voltage and current diagnostic signals. In order to study the z-dependence of the bunching, a number of shots were averaged, each having been normalized to the square root of input power. The initial incident power levels were kept near 400kW and final values are normalized to this level. Results from both electric and magnetic dipoles are plotted in Figure 4.10, where the zero axial distance corresponds to the center of the cavity gap.

Comparison with theory. A number of observations can be made from this set of runs. The rectified bunching signals should follow the sine dependence of the current modulation envelope. The agreement between the electric probe signals and this prediction is excellent, while it is slightly less good for the magnetic probes. This is probably due to a calibration error. It should be noted that the probes signals are weak, some 70 dB below the actual fields they intend to measure, making calibration to within 10 or 15%, which is the magnitude of the observed discrepancy, challenging. The distance to the bunching maximum predicted from the dispersions relation under the long wavelength approximation is shown in Figure 4.11. For the range of operating parameters and beam radius uncertainties, the distance to the modulation maximum falls between 8 and 12 cm. It is observed that this distance is a quite sensitive to a number of experimental parameters: beam current, beam radius, etc. Nevertheless, the measurements fall within the theoretical predictions.

In order to find out whether finite beam thickness effects are important in determining the distance to the bunching maximum, simulations were run with worst case

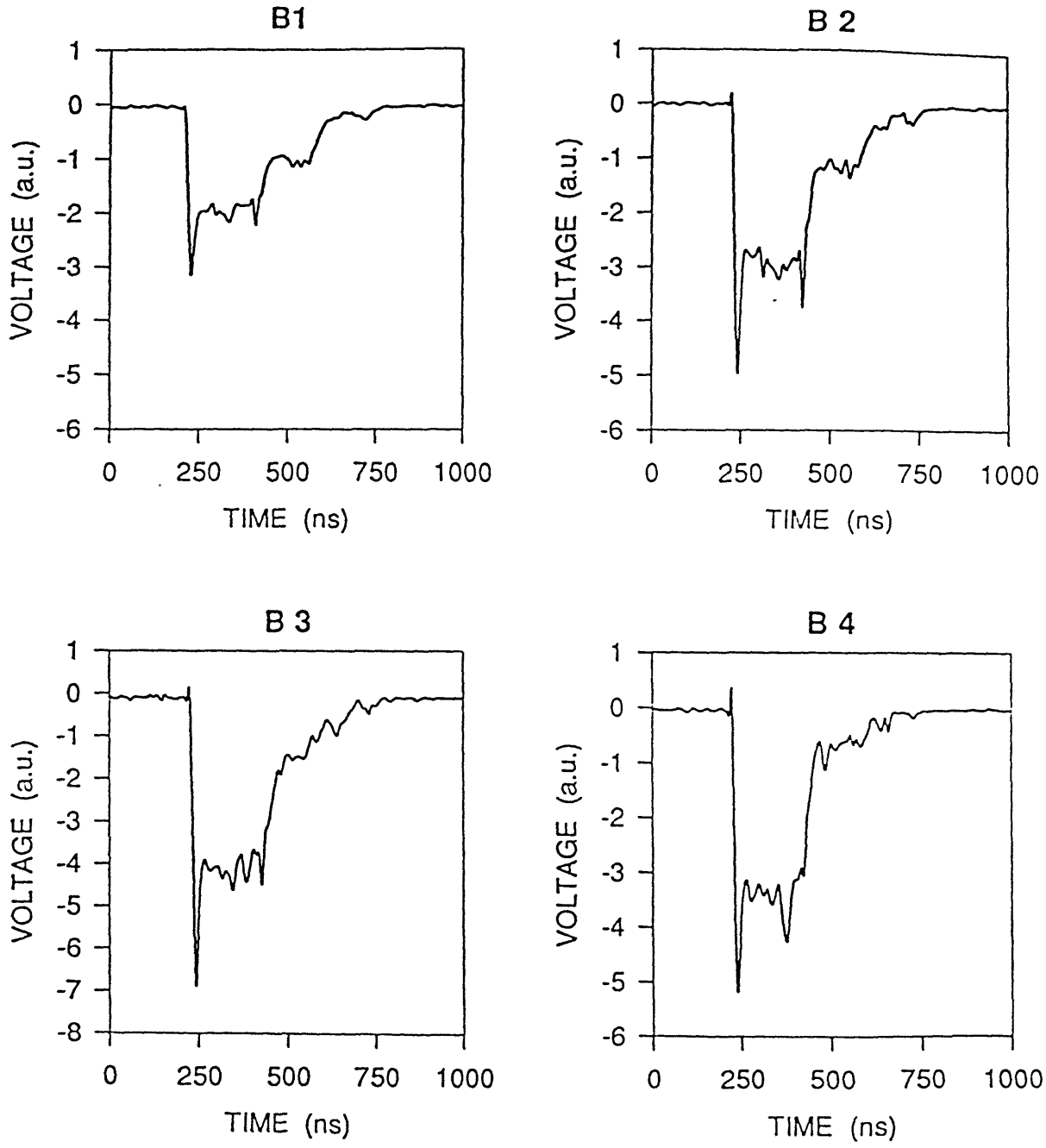

Figure 4. 9 *Time traces of magnetic probe signals at four axial positions downstream from the cavity gap. Vdio=350kV, B=10kG*

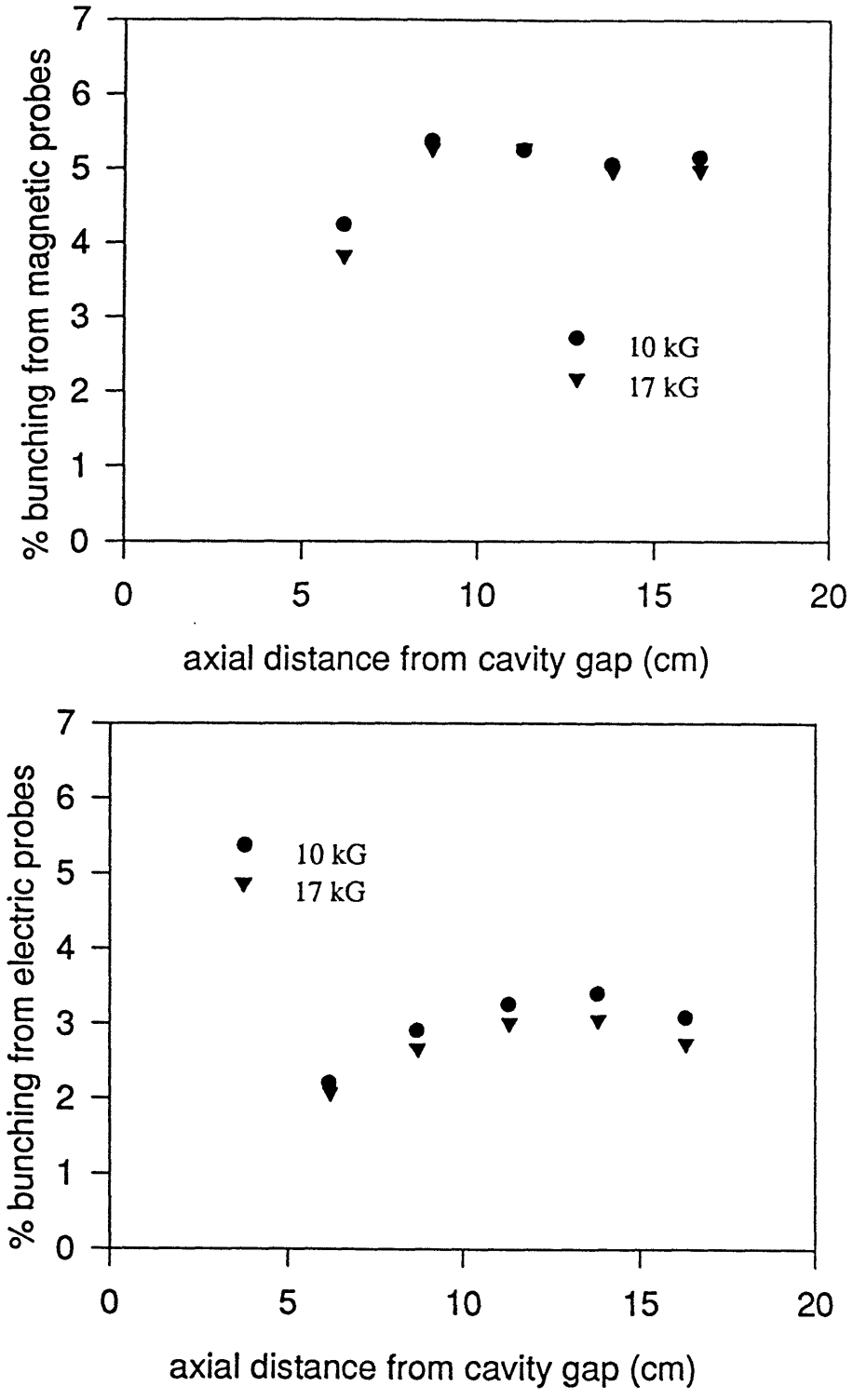

Figure 4. 10 *Axial dependence of beam bunching for 10 and 17 kG guide fields. Each point is an average of several shots, normalized to 400kW input power.*

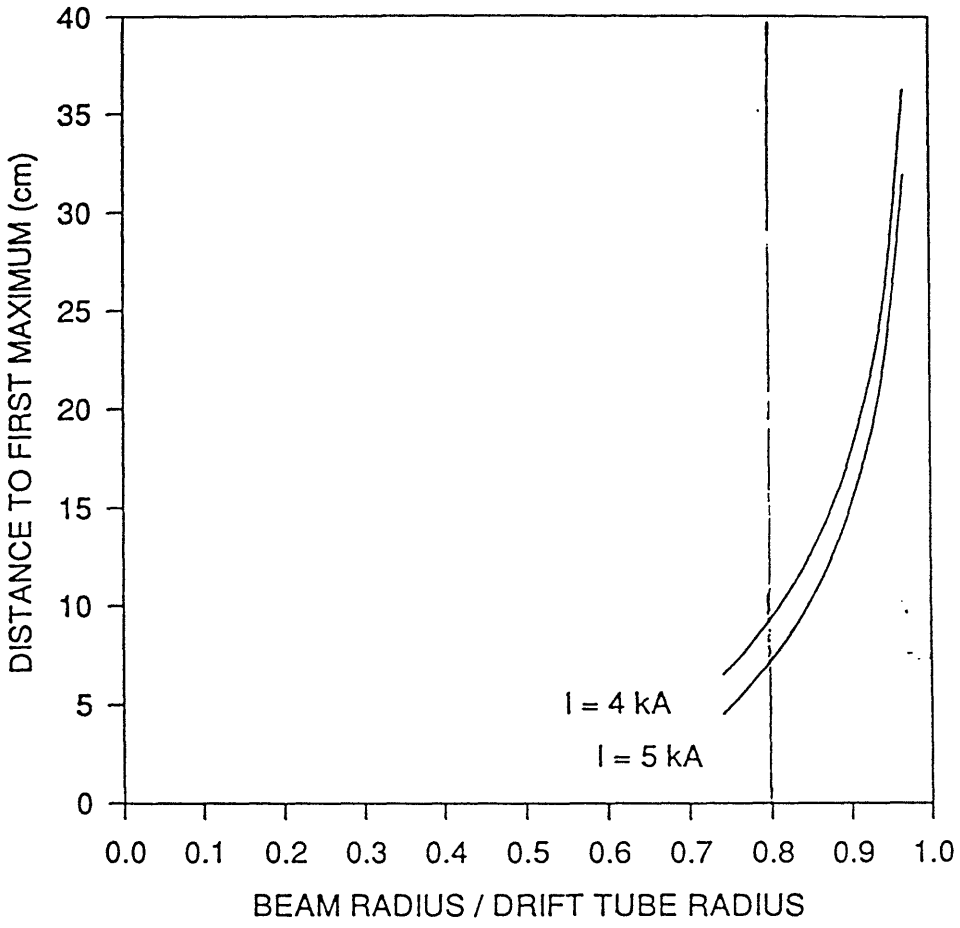

Calculated from dispersion relation for long wavelengths.
Injection energy: 350 keV

Figure 4. 11 *Calculated distance to the first bunching maximum predicted by the long wavelength dispersion relation and its sensitivity to beam radius for two beam currents.*

values for beam thickness. This value was taken as the thickness of thermal paper damage when a witness plate was placed in the beam path in the drift tube. Capable of gnawing 1/8 inch deep into graphite after 25 shots, the beam may have burned off more paper than the actual beam thickness. It is also possible that beam density profile is peaked near the mean radius, which would decrease the effective Δr. Finite gap effects are included in the simulations. However, for beams of 1 mm thickness, simulation results are close to analytic theory without gap effects. Results of a run for a 3 mm beam thickness are shown in Figure 4.12. The distance to the maximum is about 13 cm, an increase of 4 cm over that predicted by the full dispersion relation for an infinitely thin beam and 5.5 cm over the long wavelength approximation.

Bunching dependence on magnetic field. To see whether the guide magnetic field plays a role in the bunching process, experiments were performed at 1.0 and 1.7 T field strengths. Nearly identical bunching levels were observed, as can be seen from Figure 4.10, in which the axial dependence of the bunching are compared for the two guide field strengths. This shows that a 1 Tesla field is all that is required in the RKA.

Bunching dependence on beam current. The dependence of bunching on beam current was investigated by repeating the previous runs with a smaller diode gap separation. The decrease in diode impedance yields a higher beam current and slightly lower diode voltage, which reduces the bunching length. Experimental results for gap separations of 1.5 cm and 1.3 cm are shown in Figure 4.13 and show excellent qualitative

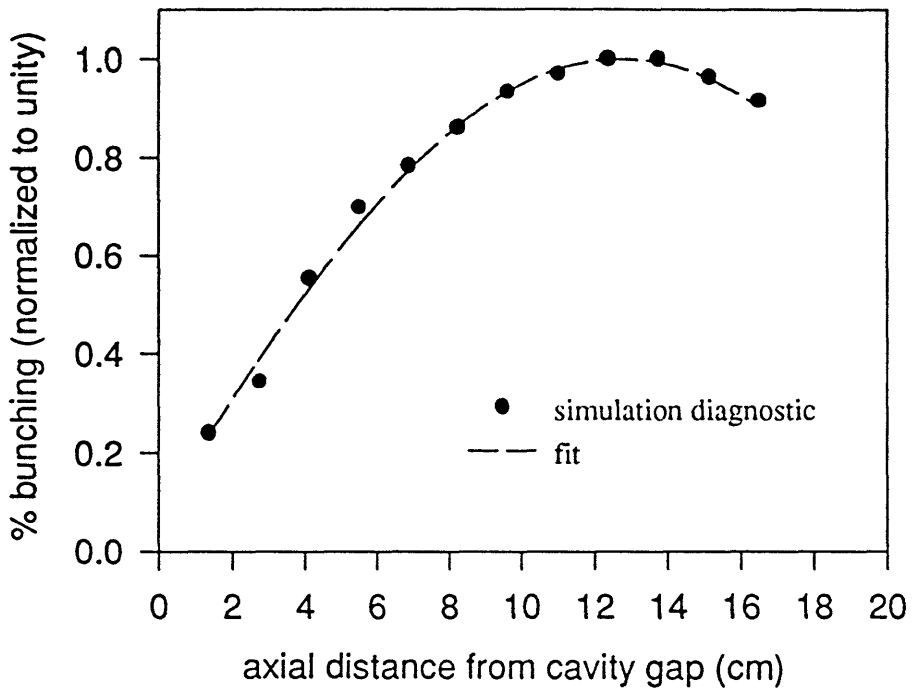

Figure 4. 12 *Amplitude of current modulation extracted from MAGIC simulation including finite beam thickness effects. a=1.89 cm, Δa=0.3cm, V_{inj}=350 kV, I_b=5 kA, f=3.4 GHz.*

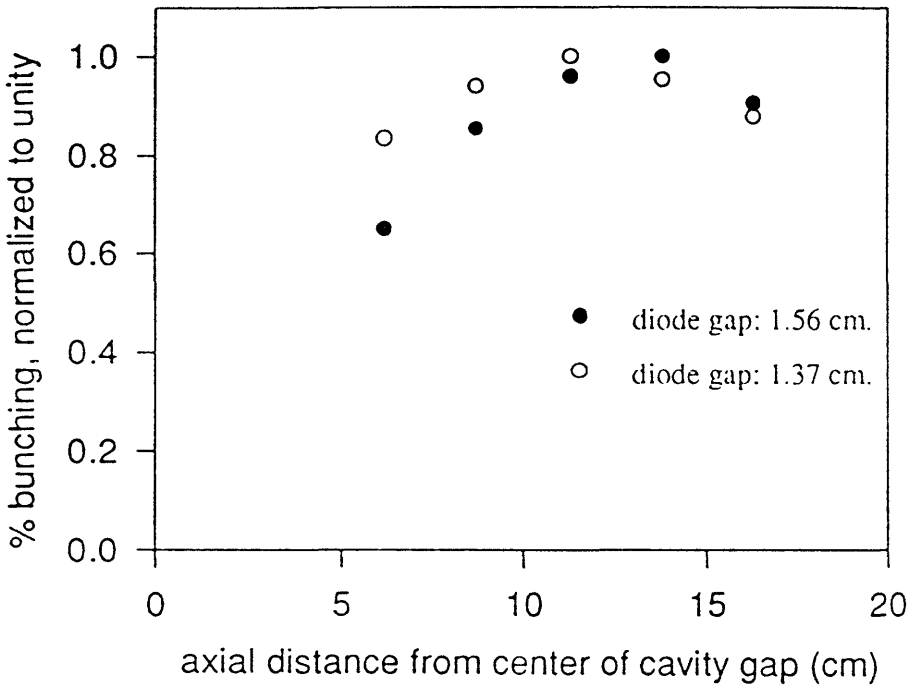

Figure 4. 13 *Experimental observation of the effect of beam current on axial dependence of current modulation. Data points are averages of several shots, normalized to unity. f=3.377 GHz.*

agreement with theory. The second set of data, which peaks earlier in z, also shows the sine dependence of the bunching more clearly.

4.3.3 Measurement of Q and reflectivity

Measurements of cavity Q and beam induced resonant frequency shifts were of interest, as they provide pertinent information for design of subsequent stages of the RKA. The tunable magnetron allowed us to track the cavity resonance for the input stage. The loaded Q of the cavity was measured by monitoring the bunching level at a fixed z position as a function of frequency. Averages of three to five shots were performed per frequency with each shot was normalized to input power. Loaded Q's measured simultaneously with electric and magnetic both a z = 11 cm are shown in Figure 4.14. MAGIC simulations were run with a 5kA beam and $Q=\omega\tau$ was computed from the fill time τ of B_θ in the cavity gap. The simulations predict a loaded Q of 35, which agrees well with the measured values of 40 to 45.

From the time dependent bunching waveforms (Figure 4.9), it can be seen that in addition to the usual temporal response, which is the level cited in all bunching results, there is a prominent spike at the start of some of the waveforms. The spike can reach up to three times the level of the flat region. Because it is characteristic of shots only very near the frequency resonance of the cavity, it cannot be a vestige attached to fast risetime of the signal. A frequency dependence plot of the spike magnitudes reveals the cold Q shown in Figure 4.15. It is possible that the spike is a real effect related to the field build

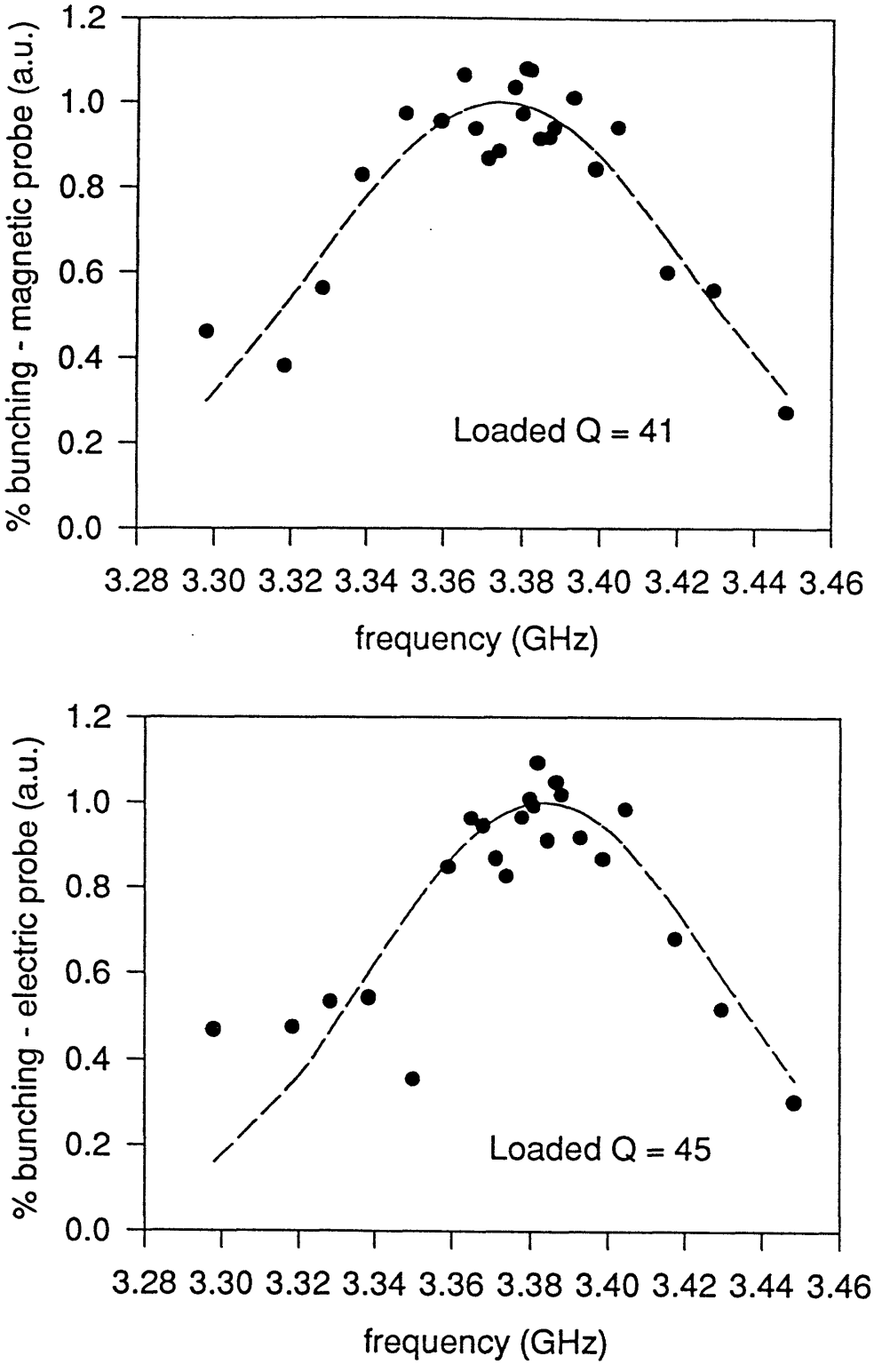

Figure 4. 14 *Loaded cavity Q measured from frequency response of electric and magnetic dipoles. I_b=5kA. Shots are normalized to input power and averaged.*

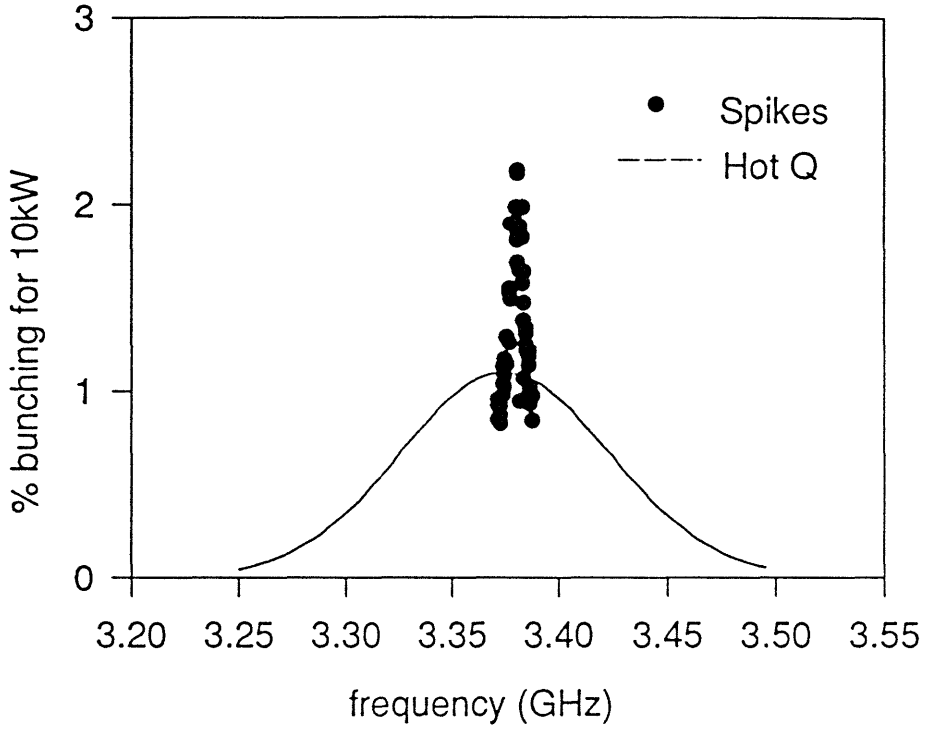

Figure 4. 15 *Spikes observed on both magnetic and electric dipoles.*

up during the fill time of the cavity. However, the effect is not reproduced by MAGIC when microwaves precede the beam by 30 ns.

Measurements of reflected power. Reflected power studies of the cavity provide useful information for improvement of the klystron wall-plug efficiency. Reflected power is measured from a directional coupler immediately preceding the cavity. Figure 4.16 compares percent reflected power under unloaded and loaded conditions. Power coupling under unloaded conditions reaches 80% at resonance. The momentary rise at the beginning of the waveform at resonance has a duration of 40 ns, which is the fill time corresponding to the measured cold Q. In the presence of the beam, the reflected power from the cavity increases to 50% at resonance. Attempts to improve this value will be described.

4.3.4 Frequency shifts

A table summarizing measured and predicted values for frequency shifts due to beam loading is included below. The dipole probes showed small frequency shifts of a few MHz down from the cold resonant frequency, while the reflected power minimum occurred 10 MHz above the cold frequency. Of the experimental measurements, the more solid are probably from the dipole probes; the reflected power measurements may be a combination of multiple effects.

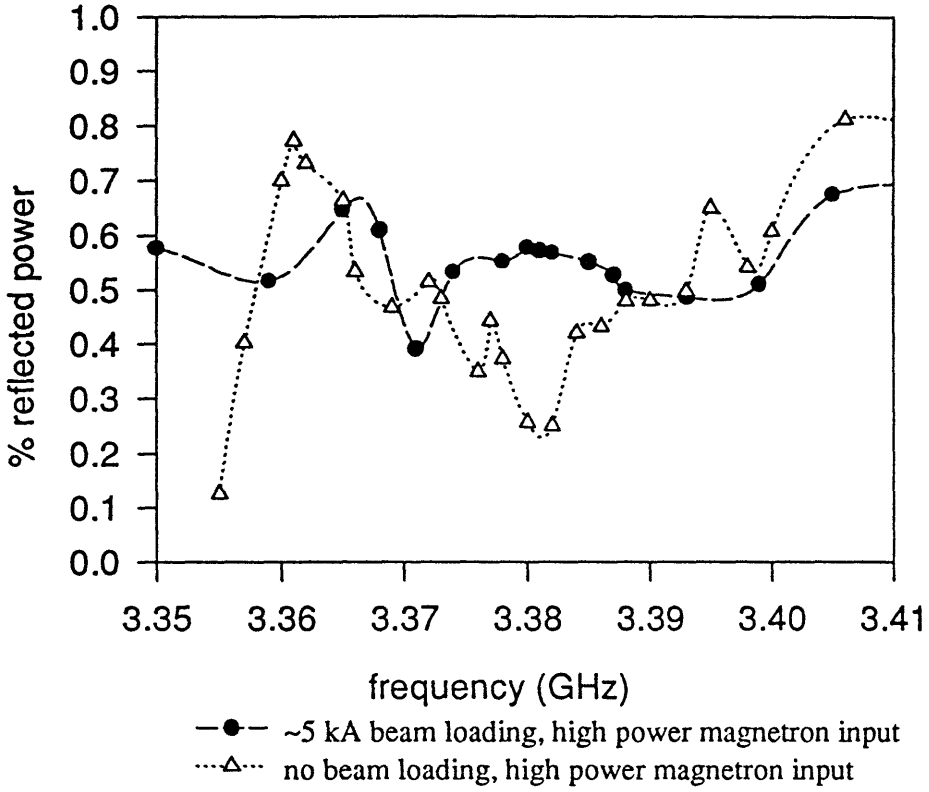

Figure 4. 16 *Percent reflected power from the cavity under loaded (I_b=5kA) and unloaded conditions.*

Table 4. 1

FREQUENCY MEASUREMENT TECHNIQUE	RESONANT FREQUENCY	FREQUENCY SHIFT
cold tests	3.383 GHz	reference
hot tests - E probes	3.384 GHz	+1 MHz
hot tests - B probes	3.374 GHz	-10 MHz
hot tests - P_{refl}	3.393 GHz	+10 MHz
simulations - cold	3.379 GHz	reference
simulations - 5kA	3.404 GHz	+25 MHz

Cavity natural frequencies were extracted from MAGIC simulations for various degrees of beam loading. Diagnostics were positioned at the center of the cavity gap. As the beam current is stepped to 6kA, the operating mode shifts upward by about 40 MHz (Figure 4.17). The 8 resonant frequencies below the operating mode are insensitive to beam loading until I_b reaches 6kA, while the operating mode increases steadily.

4.3.5 Attempts to improve efficiency - preliminary results.

A first attempt to improve power coupling to the input cavity involved the quartz window which provides a vacuum/SF_6 interface at the input port to the cavity. Over time the TE_{10} mode structure had imaged on the window as brown discoloration and fissures near the walls where the field strength is highest. It is possible that flashover and plasma formation at the window due to high field strengths could adversely affect power coupling to the cavity. Any vulnerability of the window to flashover is enhanced by its orientation parallel to the magnetic field. It is also more likely to happen in a mode with high

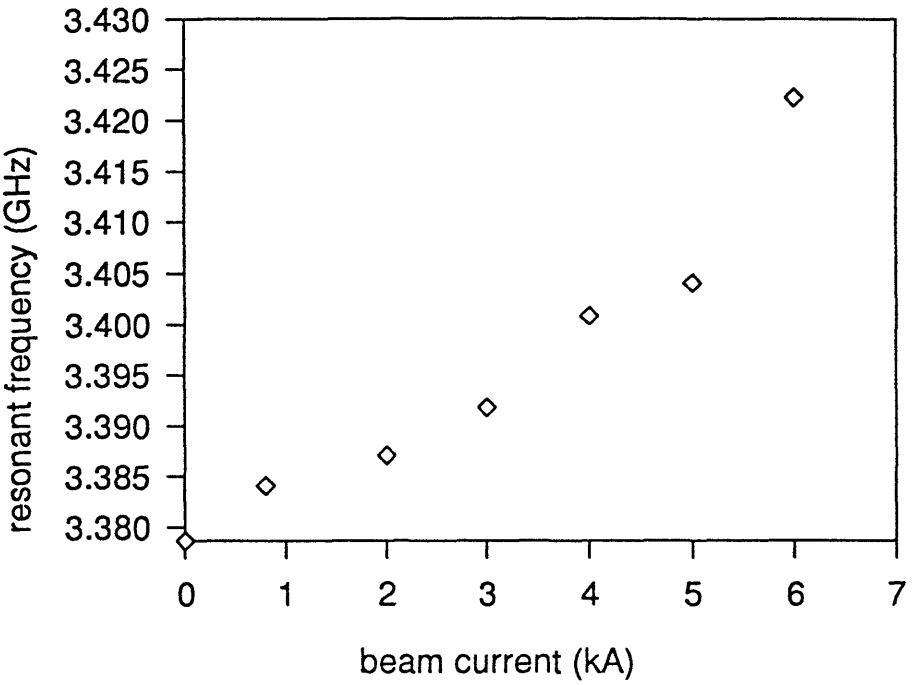

Figure 4. 17 *Resonant frequency of cavity as a function of beam loading predicted by MAGIC simulations.*

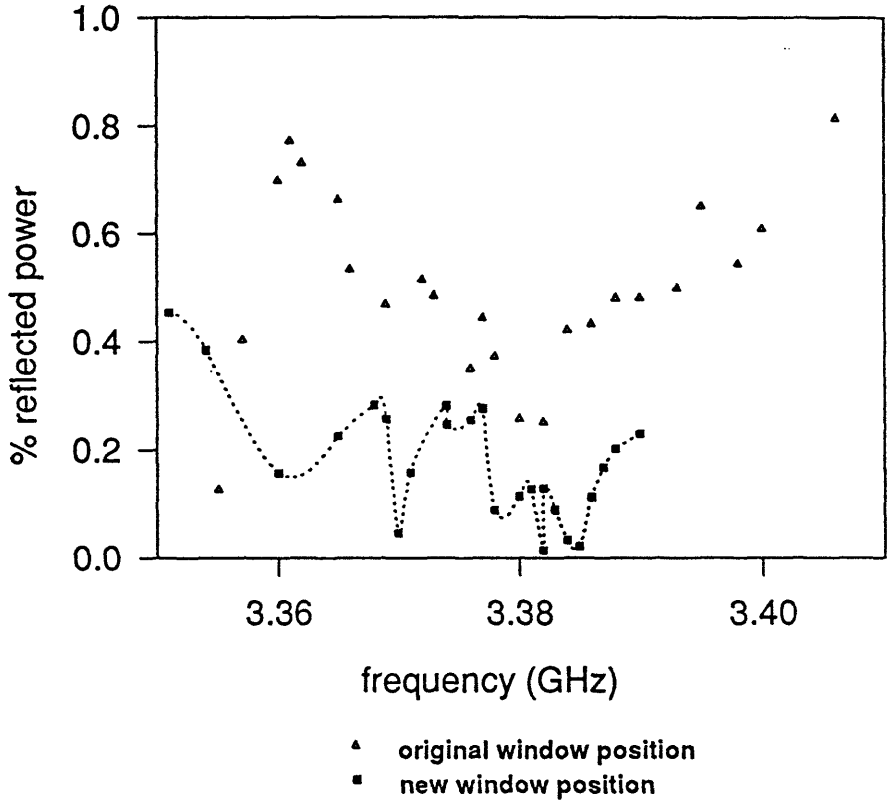

Figure 4. 18 *Comparison of the unloaded percent reflected power for the two window positions.*

azimuthal number than a uniform mode. It is not known whether the damage was incurred at the operating mode or during frequency scans in which neighboring non-uniform modes were resonant.

The quartz window was removed from the C-band input port of the cavity and a new one installed in the S-band entrance to the transition. The lower energy density at the S-band side for a given input power input reduces the risk of flashover. Preliminary measurements of reflected power for the two window positions (Figure 4.18) show an improvement. For the original window position, an large increase in the cold Q was observed from unloaded measurements taken at the mW level to unloaded measurements at 100's of kW. With the new window position, the Q has returned to its high value at high power, and the percent reflected power is much lower. The frequency dependence of loaded reflected power is still under study. A retuning of the cavity may bring further improvement. The new window position produced encouraging results overall.

CHAPTER FIVE

Conclusions

Our experimental efforts aim to build a device that will extend the boundaries of RKA technology to higher frequencies and energy outputs and further the understanding of related physics issues. Experimental work on the first stage of the RKA has been described in this thesis. We designed a reentrant input cavity resonant at 3.383 GHz in conjunction with the PIC code MAGIC, and determined its properties empirically, under both unloaded and loaded conditions. We studied the current modulation produced by the input cavity section across the parameter space and compared results with theory.

Tests on the input cavity generated useful design information for future RKA stages. The cavity configuration incorporated a number of tuning knobs, and experiments provided a feeling for their relative importance. It was found that a surprisingly simple power injection scheme was feasible. The desired operating mode was secured in spite of asymmetrical coupling, without any tuners in the cavity outer wall. A mapping of the resonant properties of the unloaded cavity as a function of cavity length culminated in an operating point a few MHz away from the simulation result.

Measurements of the beam-loaded cavity characteristics yielded the following results: Resonant frequency shifts in the initial experiments were as small as a few Mhz, although there was some discrepancy ($\pm$ 10 MHz) between frequency shifts measured by different means or following changes to the cavity set-up. Simulations predicted

somewhat larger frequency shifts than those observed empirically. The loaded cavity Q of about 40 agreed with simulations. In the presence of the beam, reflected power increased to about 50%. However, the means to improve power coupling have not yet been exhausted.

Current modulation downstream from the input cavity gap was studied as a function of numerous parameters: input power, axial position, beam current and guide field strength. The input cavity section produced about 5% current modulation. Data was recorded simultaneously with electric and magnetic dipole probes, and they performed equally well in the regime of operation. Scaling with input power, axial position and beam current was in good agreement with theory. Finally, guide field strength did not have a large impact on the magnitude of the current modulation.

REFERENCES

[Benford, 1992] J. Benford and J. Swegle, *High Power Microwaves*, Artech House, Boston, 1992, pg 347.

[Briggs, 1976] R. J. Briggs, "Space-charge waves on a relativistic, unneutralized electron beam and collective ion acceleration," Phys. Fluids **19** (8) 1257 (1976).

[Chen, 1993] C. Chen, P. Catravas, and G. Bekefi, "Growth and saturation of stimulated beam modulation in a two-stream relativistic klystron amplifier," Appl. Phys. Lett. **62** (14) 1579-1581 (1993).

[Clark, 1971] R. S. Clark, "Nereus Marx Generator, a 600 kilovolt - 1.5 kilojoule unit," Technical Report No. SC-DR-71 0216, Sandia Laboratories, (1971).

[Colombant, 1991] D. G. Colombant, Y. Y. Lau, M. Friedman, J. Krall, and V. Serlin, "Relativistic klystron amplifiers III: dynamical limiting currents, nonlinear beam loading and conversion efficiency," Proc. SPIE **1407** (1991)

[Friedman, 1985] M. Friedman and V. Serlin, "Modulation of Intense Relativistic Electron Beams by an External Microwave Source," Phys. Rev. Lett. **55** (26) 2860-2863 (1985).

[Goplen, 1991] B. Goplen, L. Ludeking, D. Smithe, and G. Warren, MAGIC User's Manual, Technical Report prepared for Air Force Office of Scientific Research, No. MRC/WDC-R-282 (1991).

[Hinshelwood, 1985] D. Hinshelwood, "Explosive Emission Cathode Plasmas in Intense Relativistic Electron Beam Diodes," NRL Memorandum Report No. 5492, (1985).

[Krall, 1991] J. Krall, M. Friedman, Y. Y. Lau, and V. Serlin, "Relativistic klystron amplifier IV: simulation studies of a coaxial-geometry RKA," Proc. SPIE **1407** (1991)

[Lau, 1987] Y. Y. Lau, "Some design considerations on using modulated intense annular electron beams for particle acceleration," J. Appl. Phys. **62** (2) 351-356 (1987).

[Lau, 1989] Y. Y. Lau, J. Krall, M. Friedman and V. Serlin, "On certain theoretical aspects of relativistic klystron amplifiers," SPIE **1061** 48 (1989).

[Lau, 1990] Y.Y. Lau, M. Friedman, J. Krall, V. Serlin, "Relativistic Klystron Amplifiers Driven by Modulated Intense Relativistic Electron Beam," IEEE Transaction on Plasma Science **18**, (3) 553-569 (1990).

[Ullschmied, 1993] Conversation with J. Ullschmied.